AN ABSTRACT OF THE THESIS OF

Vishal Patil for the degree of Master of Science in Mechanical Engineering presented on March 16, 2005.

Title: Application of Infrared Thermography for Temperature Measurement in Microscale Internal and External Flows.

Abstract Approved:

Redacted for Privacy

Vinod Narayanan

Infrared (IR) thermography is applied to estimate heat transfer rates in external and internal microscale convective flows. The technique and analysis are developed in the context of external jet impingement flow and internal single-phase liquid flows.

A heated-thin-foil thermography technique is applied to perform surface temperature visualization on a submerged 125-μm circular microscale jet impingement. Microscale jets flows are associated with low exit Reynolds number (Re) due to the small characteristic length of the nozzle, but correspondingly high exit velocities, and hence, a high subsonic Mach number. Detailed distributions of heated and adiabatic wall temperature, and local and average Nusselt number (Nu) variations are presented for a single 125-μm diameter air jet impingement for five laminar exit Re in the range of 690 to 1770 at three nozzle-to-surface spacing of 2, 4, and 6 times

the nozzle diameter. The corresponding jet exit Mach numbers vary between 0.26 and 0.63. Lateral heat conduction along the impingement surface is significant and warrants inclusion in the calculation of heat transfer coefficient. Results indicate that the adiabatic surface temperature distribution is relatively insensitive to nozzle-to-surface spacing within the parameter range studied. With an increase in Re, the adiabatic surface temperature decreases significantly near the stagnation point. The average Nu is higher compared to the turbulent macroscale Martin's correlation for large Re.

A technique for quantitative temperature visualization of single-phase liquid flows in silicon (Si) microchannels using infrared thermography is presented. This technique offers a new way to measure, non-intrusively, local variations in wall temperature, or fluid temperature at the fluid-wall interface, in a microchannel fabricated entirely of silicon. The experimental setup and measurement procedure required to obtain high signal-to-noise ratio is elaborated.

A single 13-mm long, 50 μm wide by 135 μm deep Si microchannel was used in this study. Experiments were performed with a constant electrical heat input rate to the heat sink surface for four fluid flow rates between 0.6 g/min and 1.2 g/min, corresponding to a Re range from 200 to 300. The estimated experimental fully developed Nu compares reasonably well with the solution provided in literature for laminar flows. Results indicate that axial non-uniformity can be significant for the large Peclet number flows.

Application of Infrared Thermography for Temperature Measurement in Microscale Internal and External Flows.

by

Vishal Patil

A THESIS

submitted to

Oregon State University

in partial fulfillment of
the requirements for the
degree of

Master of Science

Presented March 16, 2005
Commencement June 2005

Master of Science thesis of Vishal Patil presented on March 16, 2005

APPROVED:

Redacted for Privacy

Major Professor, representing Mechanical Engineering

Redacted for Privacy

Head of the Department of Mechanical Engineering

Redacted for Privacy

Dean of the Graduate School

I understand that my thesis will become part of the permanent collection of Oregon State University libraries. My signature below authorizes release of my thesis to any reader upon request.

Redacted for Privacy

Vishal Patil, Author

ACKNOWLEDGMENTS

I would like to acknowledge my major advisor, Dr. Vinod Narayanan, for all his support, motivation and expertise provided in the completion of this work. Also I am grateful to Dr. Liburdy, Dr. Kanury and Dr. Skyllingstad for agreeing to serve on my committee.

Finally, I extend my thanks to my teachers and colleagues with whom I shared many insightful discussions on this subject matter.

TABLE OF CONTENTS

TABLE OF CONTENTS (Continued)

LIST OF FIGURES

LIST OF TABLES

LIST OF APPENDICES

LIST OF APPENDIX FIGURES

LIST OF APPENDIX TABLES

APPLICATION OF INFRARED THERMOGRAPHY FOR TEMPERATURE MEASUREMENT IN MICROSCALE INTERNAL AND EXTERNAL FLOWS

CHAPTER 1: MOTIVATION

In recent years, miniaturization of electronic components has lead to high cooling demands on heat sinks. This has generated a great interest in microscale flows. Knowledge of local flow and heat transfer characteristics will aid in understanding the physics of these flows and ultimately in designing the micro heat sinks more effectively. However, measurement of local wall temperature to determine the local heat transfer characteristics has been a challenge to researchers. This thesis presents a non-intrusive method to estimate heat transfer rates in microscale flows.

Infrared (IR) thermography is a well established measurement technique in macroscale heat transfer research (Carlomagno and deLuca, 1989; Hestroni et al., 1996, Sargent et al., 1998; Astarita et al., 2000). However, far-field IR thermography has received little or no attention for temperature measurement in microscale flows. Near-IR particle image velocimetry has been studied recently to determine velocity distributions in microchannel flows (Chung et al., 2001; Han et al., 2004; Liu et al., 2004). The ability to obtain, non-intrusively, detailed temporal and spatial local surface temperature measurements are distinct advantages of IR thermography.

This thesis documents the use of infrared thermography to perform detailed surface temperature visualization on microscale flows. The IR technique is successfully applied to determine local heat transfer characteristics of microscale air jet impingement (Chapter 3) and single phase liquid flows through all-silicon microchannels (Chapter 4).

CHAPTER 2: AN OVERVIEW ON INFRARED DETECTORS

This section presents a brief overview of infrared (IR) detectors. More exhaustive information can be found in Rogalski (2002) and Horny (2003).

IR detectors can be classified based on the basis of their principle of operation as photon and thermal detectors. In case of photon detectors, the radiation is absorbed within the material by interaction with electrons which in turn gives an electrical output signal. The photon detectors show selective wavelength dependence in radiation absorbance and hence in their response to radiation absorbed. They exhibit good signal to noise ratio and fast response. However, they typically require cooling which makes them bulky, heavy, expensive and inconvenient to use.

In thermal detectors, incident radiation is absorbed to raise the temperature of the material which in turn causes a physical property of the material to change. This change is used to generate an electrical output. The radiation absorbance of the detector is generally wavelength independent. This type of IR detector, when compared with photon detector, is inexpensive and easy to use but has modest sensitivity and slow response.

IR detectors can be further classified as a single sensor detector and detector with matrix of sensors called focal plane array (FPA) detector (Rainieri et al., 2001). In a single sensor detector, the radiation emitted by a object is recorded sequentially by scanning at a given frequency line by line the whole field of view. This is usually done using a mechanical device like a rotating prism. This type of detector introduces noise, due to this scanning mechanism, in the measurement. However, it is more effective than FPA detector in eliminating unwanted radiation from the surroundings. The FPA detector has a matrix of sensors which instantaneously records the radiation emitted from the field of view. This type has raised the spatial resolution and sensitivity of the IR cameras. However FPA detector introduces more noise as compared to single sensor detector due to its drawback of receiving unwanted flux from the surroundings. This drawback can be eliminated by a careful calibration of the camera (Rainieri et al., 2001).

The IR imaging system (CMC Electronics, TVS 8500), used for the present study, is a mid-wavelength (3.5 – 5.1) μm range imager which consists of a front-illuminated 256 x 256 InSb focal plane array of photovoltaic type detectors, cryogenically cooled by an integrated Stirling cooler to ensure high sensitivity and low-noise measurement. With a microscope lens, the camera can measure intensity (and temperature) distributions at 65,536 locations in an area of 2.56 mm x 2.36 mm, at a maximum rate of 120 frames per second. For a known emissivity of the test article, the resolution of temperatures recorded in these micro-channels could be better than 50 mK per the manufacturer's specification.

CHAPTER 3: MICROSCALE JET IMPINGEMENT

3.1: INTRODUCTION

This chapter documents specific considerations required for determining heat transfer rates of an external microscale convective flow from a proper analysis of surface temperature data obtained using the heated-thin-foil thermography. In particular, the experimental procedure and analysis are developed in the context of a submerged circular microscale jet impingement flow. Typically, microscale flows are associated with large temperature gradients, and it is important to note its implications on the experimental technique. Contribution of lateral heat conduction within the foil, which can be neglected in macroscale flows, becomes dominant in microscale studies.

Spatially-resolved heat transfer rates of a 125-μm impinging air jet are presented. The jet flow, created by a single 125-μm circular tube, impinges onto a heated flat surface placed normal to it. Five exit Re ranging from 690 to 1770 are investigated at three nozzle-to-surface spacings (H) of 2, 4, and 6 nozzle diameters (D). The corresponding Mach number (M) varies from 0.26 to 0.63. Local surface temperature measurements are performed non-intrusively using IR thermography.

3.2: NOMENCLATURE

A Sound speed in air (m/s)

A_{foil} Area of the heated foil (m^2)

A_i Convective area of the i^{th} control volume (m^2)

D Nozzle exit diameter (m)

H Distance between nozzle exit and impingement surface (m)

h_i Local heat transfer coefficient (W/m^2-K) for the i^{th} control volume

$h_{av,i}$ Average convective heat transfer coefficient over a convective area of radius r_i (W/m^2-K)

I Current passed through the foil (A)

k Thermal conductivity of the foil (W/m-K)

k_{air} Thermal conductivity of air (W/m-K)

ℓ Length of the foil (m)

M Mach number ($M = V_{exit}/a$)

Nu Local Nusselt number ($Nu = h_iD/k_{air}$)

Nu_{av} Average Nusselt number

P_o Pressure in the plenum (kPa)

$\dot{Q}$ Flow rate at the nozzle exit (m^3/s)

q_{gen} Heat generated in the foil (W)

q_{cond} Heat conducted in the foil (W)

q_{rad} Heat radiated from the foil (W)

R Recovery factor

R_{foil} Resistance of the foil (ohms)

r Radial distance from stagnation point (m)

Re Reynolds number ($Re = V_{exit}D/\nu$)

Re_H Reynolds number based on H

t Thickness of the foil (m)

T Temperature of the heated foil (°C)

T_o Total plenum temperature (°C)

T_s Static jet exit temperature (°C)

T_{surr} Surroundings Temperature (°C)

T_{aw} Adiabatic foil Temperature (°C)

T^*	Non-dimensional temperature of the heated foil $[T^* = (T+273.15)/(T_o+273.15)]$
T^*_{aw}	Non-dimensional temperature of the foil $[T^*_{aw} = (T_{aw}+273.15)/(T_o+273.15)]$
V_{exit}	Velocity at the jet exit (m/s)
w	Width of the foil (m)

Greek

ε	Combined emissivity of the upper and lower foil surface
ν	Kinematic viscosity (m^2/s)
σ	Stefan Boltzmann constant (5.67×10^{-8} W/m^2-K^4)

3.3: LITERATURE REVIEW

Most microscale multiphase fluidic and thermal heat sinks used for electronics cooling and other high heat flux cooling applications eventually need to reject heat to the ambient surroundings. The overall size of a microscale thermal transport system incorporating such heat sinks thereby depends on the rate at which heat can be transported by the integrated system to the surroundings. Microscale air jets can be used to enhance heat transfer rates in the low heat transfer side of such systems; hence, there is a need to study their transport characteristics. A plethora of detailed experimental and numerical studies on macroscale axisymmetric and two-dimensional submerged impinging air jets exist in current jet literature (Martin, 1977; Viskanta, 1993). However, investigations on microscale jet impingement are sparse.

Lin et al. (2000) determined the local and average heat transfer rates associated with a 500-μm circular jet impingement onto a quartz substrate. The impingement side of the substrate was integrated with thin-film temperature sensors distributed radially, and a thin-film heater deposited on the backside provided a constant heat flux surface. For a nozzle-to-surface spacing of a unit diameter, results from their study indicated that the peak in heat transfer coefficient was shifted away from the impingement point for a turbulent Re of 2,900 while no such shift was observed for laminar jets.

Pence et al. (2003) performed a numerical study on the flow field and heat transfer rates associated with a 100-μm compressible impinging circular jet. They suggested that the high acceleration in the developing wall jet past impingement resulted in a slip flow and temperature jump at the wall for microscale jets since the

Knudsen number, based on the thickness of the viscous boundary layer, was approximately 0.01. Local Nusselt number (Nu) profiles indicated an off-center peak, while the average values were higher than that determined by Martin's correlation (Martin, 1977) for the high Mach number (M) flows. The differences were attributed to the non-continuum and compressibility effects.

The numerical studies of Pence et al. (2003) clearly indicate that a direct scaling of macroscale impinging jet heat transfer correlations (Martin, 1977) to the microscale is inappropriate since the flows are dynamically dissimilar. A low Re with a correspondingly high M is observed in microscale jets due to the small characteristic length scale and high nozzle exit velocity respectively. For an air jet, based on the limits of laminar flow in a tube (Re = 2,000) and incompressibility (M $\leq$ 0.3), a limiting jet exit diameter of approximately 300 μm is obtained below which there is an existence of a laminar and compressible flow region. This suggests that the flow field and heat transfer rates for all jets larger than 300 μm, which includes those studied by Lin et al. (2000), can be determined by a direct application of results and observations from studies in the present literature (such as in Martin (1977)).

3.4: EXPERIMENTAL FACILITY

Figure 3.1 shows a schematic of the jet impingement facility used for this study. A dedicated air compressor located in a separate room supplied compressed air, which was directed into a settling tank through filters and a pressure regulator. The flow pressure was further regulated downstream of the tank. The volumetric flow rate was measured using a calibrated rotameter (Gilmont instruments GF-7660) and controlled using a micrometer needle valve. A 2.03-mm inner diameter stainless steel tube formed the plenum. Pressure and temperature were measured in the plenum. A band heater located upstream of flowmeter was used to maintain the plenum temperature equal to temperature of the surroundings. The plenum and nozzle assembly was located on a precision 3-axis manual traversing system. The jet was created by air flow exiting a 125-μm inner diameter stainless-steel tube with a pipe length-to-nozzle-diameter (L/D) ratio of 200 which was sufficiently large to ensure a fully developed flow at the nozzle exit. The outer diameter of the tube, which was 12.7-times its inner (nozzle) diameter, partially confined the jet flow.

A schematic of the jet impingement test section is shown in Fig. 3.2. The test section consisted of a 13 mm x 3 mm, 25.4-μm-thick inconel foil attached at its ends to a 38.4-mm diameter, 3-mm-thick calcium fluoride glass window. The backside of the foil was painted flat black to provide a diffuse, high-emissivity surface for the IR detector. A direct current power supply (Tektronics PS2520G) provided a uniform heat generation in the foil. The moderate specific resistivity of inconel (103×10^{-6} Ω.cm) ensured adequate heat generation with the available dc power supply, while its relatively low thermal conductivity of 14.9 W/m-K minimized lateral heat conduction within the foil.

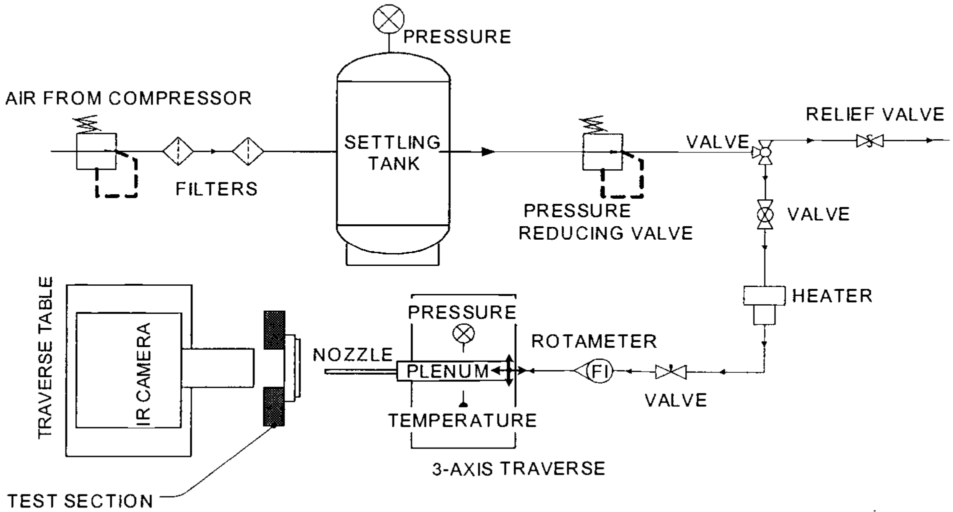

Fig. 3.1: Schematic of the microjet impingement test facility

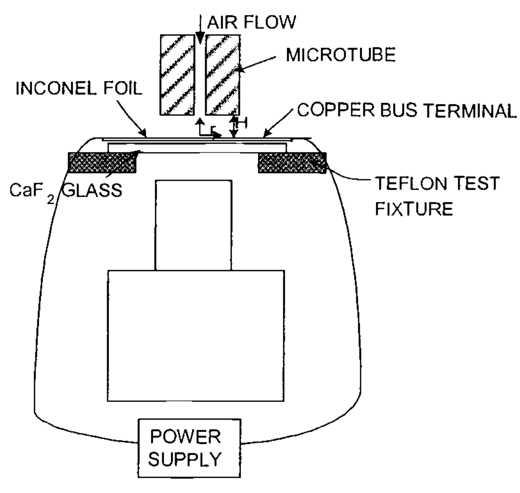

Fig. 3.2: Schematic showing details of the test section

Calcium fluoride, CaF_2, was chosen as a material for the window primarily because of its high transmissivity, τ, to radiation in the range of 0.3 to 7 μm ($\tau \approx 0.92$ for temperatures near ambient). It also served to keep the foil flat and free from deflections. The thermal contact resistance between CaF_2 glass and the foil was estimated by performing a separate experiment in which a polished inconel foil was attached at its ends to a CaF_2 glass window with the upper side painted black. The contact resistance was found to be 0.0265 $^{\circ}Cm^2/W$. The lowest convective heat transfer coefficient in region of interest for conditions studied was found to be 1450 W/m^2-$^{\circ}C$. The ratio of these two thermal resistances show that the heat flow rate into the CaF_2 window was at least 39 times lower than that removed from the top surface, indicating little energy redistribution within CaF_2 window. In addition, by a one-dimensional thermal resistance model, the heat rate through the bottom surface of the window was estimated to be less than 0.3% of that from the upper side of the foil. Hence, it was reasonable to assume a near-adiabatic boundary condition at the bottom surface of the window. The IR camera in current setup was mounted on a two-axis traverse table to facilitate independent adjustment with respect to the nozzle and the foil.

3.5: EXPERIMENTAL PROCEDURE

The perpendicularity of the nozzle to the camera was confirmed by inspecting a thermal image of the nozzle without the foil. This image was also used to locate the center of the nozzle. The foil was then located between the nozzle and the camera and a second thermal image of the foil was recorded. A foil with a focused image at all corners was considered perpendicular to the camera. The above procedure ensured normal jet impingement on the foil. This unheated image of the foil under no-flow conditions was also used to determine spatial variations in emissivity and transmissivity of the painted backside of the foil and CaF_2, respectively, which were used to correct all subsequent raw thermal images recorded. For different test conditions of H/D and Re, adiabatic images of the unheated foil with jet impingement were recorded at steady state. The foil was heated, and again, the heated thermal images of the foil were recorded at steady state. A steady state was considered to be attained when the temperature fluctuations detected by IR camera were less than 0.5°C. An average of thirty adiabatic and heated thermal images, recorded at 30 Hz at each test condition was used for further analysis. Electrical energy input was determined using current measured at the power supply and the foil resistance. A calibration experiment was performed to measure resistance of the foil, without jet impingement, by measuring voltage across the foil for varying input current settings (Appendix A).

3.6: DATA ANALYSIS

A typical adiabatic steady state thermal image of the foil caused by the impinging jet at Re = 1620 is shown in Fig. 3.3. The nozzle was located at a H/D = 4 from the impingement surface. The thermal image indicates little circumferential variation and hence, further data are presented along a radial line at different non-dimensional locations, r/D, by circumferentially averaging temperature data at equidistant pixels from the stagnation point.

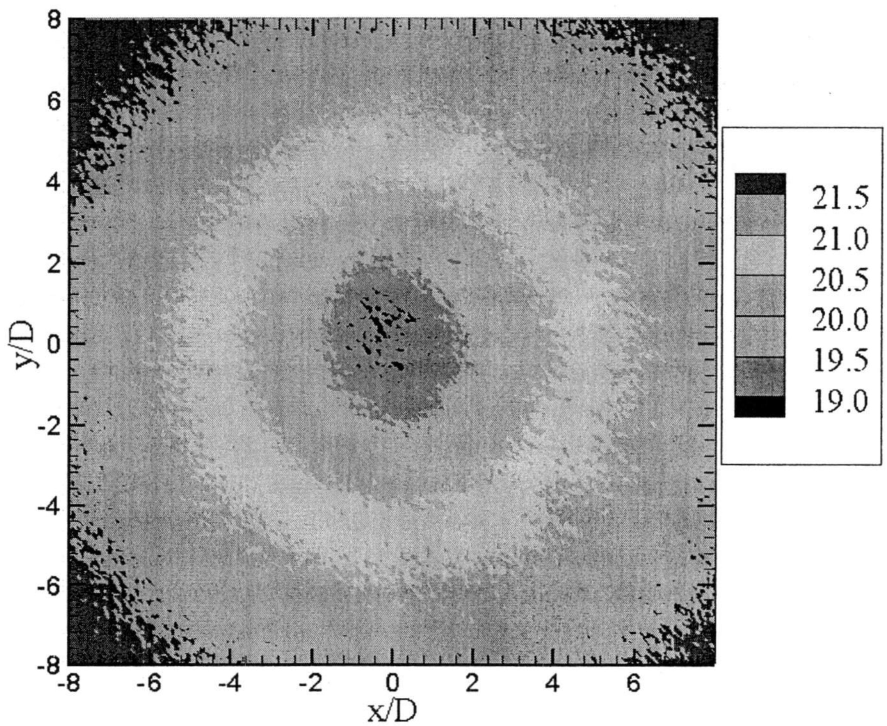

Fig. 3.3: A typical contour image of the adiabatic wall temperature distribution (in ^{o}C) for Re = 1620 and H/D = 4.

The jet exit M, and static temperature, T_s, were determined using a Fanno flow model for the microtube. Use of this model is justified based on the low value of thermal conductivity of stainless steel and large wall thickness of the steel tubing compared to its inner (jet) diameter. Preliminary experiments were performed by attaching a thermocouple on the outerside of the nozzle wall close to the exit to determine the amount of heat transferred into the nozzle. Results indicated a 1.3°C lower wall temperature for the nozzle wall compared with ambient air for the highest Re. This small temperature drop provided a small heat transfer rate into the microtube and it can be readily shown that the change in M occurred primarily due to fluid friction and not heat transfer. Pressure at the nozzle exit was considered atmospheric and an isentropic expansion was assumed between the plenum and the inlet of the microtube. The Mach number in the plenum was typically very low. Entrance loss between the plenum and the microtube was determined to be negligible compared with the drop in pressure across the steel tube and hence neglected. The net pressure drop across the tube accounting for the entrance and exit minor losses was within 2 percent of that obtained without losses, and their inclusion did not produce a noticeable change in M.

Table 3.1: Jet exit Mach numbers and static temperatures for different Reynolds numbers. (T_o = 297 K)

Re	M	T_s (°C)
690	0.26	20
970	0.36	16.6
1430	0.53	8.24
1620	0.58	5.3
1770	0.63	2.33

Table 3.1 summarizes the calculated exit M and static temperature for each experimental flow condition. It is clear that the jet flow is expected to be compressible for all but the lowest Re.

In the results presented, adiabatic wall temperatures are made non-dimensional by the jet stagnation temperature, or are represented as a local recovery factor, R_i, defined for an ideal gas as

$$R_i = \frac{T_{aw,i} - T_s}{\left(U_j^2 / 2c_p\right)} = \frac{T_{aw,i} - T_s}{T_o - T_s} \tag{3.1}$$

where U_j is the jet exit velocity, and c_p is the specific heat of air at constant pressure. The recovery factor is a common way to represent the viscous dissipation and variable property effects in high speed flows, and has been frequently used in the context of jet impingement (e.g., Goldstein et al., 1986; Meola et al., 1995). Heated wall temperatures are made non-dimensional with T_o.

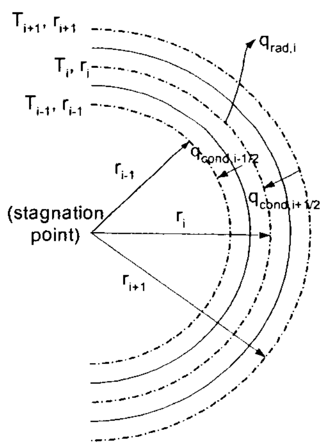

Fig. 3.4: Arrangement of control volumes

The local convective heat transfer coefficient, h_i, was determined by performing an energy balance on annular control volumes of unit thickness, indicated by the solid lines in Fig. 3.4. In this figure, the dashed lines correspond to temperature pixel locations. The local convective heat transfer coefficient for the i^{th} control volume, h_i, was determined as a ratio of the total heat removed by the convective jet flow and the difference between the local heated and adiabatic surface temperatures,

$$h_i = \frac{q_{gen} + q_{cond} - q_{rad}}{A_i\left(T_i - T_{aw,i}\right)} = \frac{q''_{gen} + q''_{cond} - q''_{rad}}{\left(T_i - T_{aw,i}\right)} \tag{3.2}$$

where q''_{gen}, q''_{cond}, and q''_{rad} represent heat flux rates based on convective area, A_i of the control volume. A positive sign convention for the energy terms indicates that net heat is transferred by that mode into the control volume. Note that heat transfer by natural convection from the topside of the foil was negligible and has been excluded in Eq. (3.2). The convective area of the i^{th} control volume, A_i, is given by

$$A_i = \pi\left(\left(\frac{r_{i+1} + r_i}{2}\right)^2 - \left(\frac{r_i + r_{i-1}}{2}\right)^2\right) \tag{3.3}$$

The rate of thermal energy generated within, net lateral heat conduction rate into, and radiated heat rate from the annular control volume respectively are calculated using

$$q_{gen} = q'''_{gen} A_i\, t = \frac{I^2 R}{w \ell t} A_i\, t, \tag{3.4}$$

$$q_{cond} = 2\pi k t \left\{ \left(\frac{r_{i+1} + r_i}{2} \right) \frac{dT}{dr}\bigg|_{i+1/2} - \left(\frac{r_{i-1} + r_i}{2} \right) \frac{dT}{dr}\bigg|_{i-1/2} \right\} \quad (3.5)$$

$$q_{rad} = \varepsilon_i \, \sigma A_i \left(T_i^4 - T_{surr}^4 \right) \quad (3.6)$$

The thermal energy generation rate, q''_{gen}, was maintained constant at 5455 W/m^2 for all experiments. The heat loss through radiation, q''_{rad} term was small since the foil was heated by less than 10 °C above ambient. The magnitude of the conduction heat flux rate, q''_{cond}, was estimated by performing an order of magnitude estimate on Eq. (3.5). For the order analysis presented in this section, a value in the range of 0.5 to 4.9 units was considered to be of order 10^0 unit, a value in range of 5 to 49 units was of order 10^1 unit, and so on. The order of the temperature gradient was determined by representing it in terms of a non-dimensional temperature gradient $d\theta/dr^*$ of unit magnitude,

$$\frac{dT}{dr} = \frac{\left(T_{max} - T_{min}\right)}{2.5D} \cdot \frac{d\theta}{dr^*} \quad (3.7)$$

In Eq. (3.7), the local temperature of the foil was made non-dimensional by the difference between the maximum and minimum temperatures T_{max} and T_{min} respectively in the region of interest

$$\theta = \frac{\left(T - T_{min}\right)}{\left(T_{max} - T_{min}\right)} \quad (3.8)$$

The radius of the region of interest was made non-dimensional by 2.5 times nozzle diameter based on the practical limits beyond which multiple jet arrays can be considered necessary (see Fig. 3.11 for Nu profiles).

In this experiment, (T_{max} - T_{min}) and D were of orders 10^0 °C and 10^{-4} m respectively, resulting in an order of 10^4 °C/m for dT/dr. Similarly, from Eq. (3.3), A_i was of order 10^{-8} m^2. Thus, from Eq. (3.5), q''_{cond} was of order 10^4 W/m^2, whereas q''_{gen} was also of order 10^4 W/m^2. This indicates that lateral conduction heat flux rate contributed a significant portion to the net heat coming into the control volume. Hestroni et al. (1996) performed a similar analysis while applying the heated thin-foil technique to wall temperature fluctuations in a turbulent channel flow. They determined that the lateral heat conduction along the foil could be neglected provided the non-dimensional term, $4kt/h_{av}d^2$, was much smaller compared to unity. In their terminology,'d' represented the diameter of the spot of temperature heterogeneity, which emerged due to the turbulence/wall interaction and h_{av} was the average convective heat transfer coefficient over the spot. Clearly, this non-dimensional term was substantial in our study due to the small region of interest and could not be neglected. One way to minimize this effect would be to use a low thermal conductivity foil material or/and a thinner foil. This could reduce the order of lateral conduction to about 10^3, which would still be considerable.

Since the radial temperature gradients were large (of order 10^4), it was important to reduce the noise in the raw temperature data by using a high-order polynomial curve fit. A typical curve fit of experimental data points of heated wall temperature with radial location from the jet centerline is shown in Fig. 3.5 for a Re of 1770. The raw temperature data from r = 0 to 6D was mirrored about r = 0 and then curve fitted using Tablecurve 2D® software. Mirroring of data ensured that dT/dr of curve fitted data was equal to zero at stagnation point. This condition was enforced to eliminate spurious high values of q''_{cond} that could result from large temperature gradients around the stagnation point. Also this condition was true physically as r = 0 corresponded to the axis of symmetry. Once the temperature data points were curve fitted, the derivatives were generated at required radii and q''_{cond} was determined using Eq. (3.5).

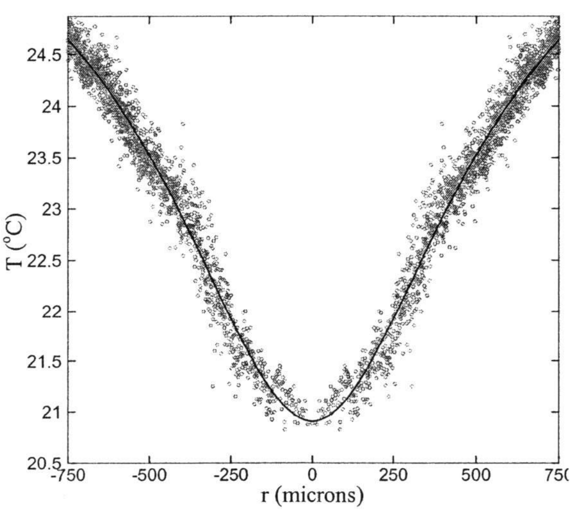

Fig. 3.5: Curve fit of experimental data (for Re = 1770 and H/D = 4)

Figure 3.6 shows radial distribution of non-dimensional heated wall temperature profiles for different Reynolds numbers at H/D of 4. As seen in the figure, the temperature gradients around the impingement point increased with Re. This resulted in a corresponding high rate of lateral conduction along the foil towards the stagnation point for large Re flows. The radial distribution of q''_{cond} is shown in Fig. 3.7 for various Re at H/D of 4. Note that the magnitude of q''_{cond} is consistent with the order estimate presented earlier.

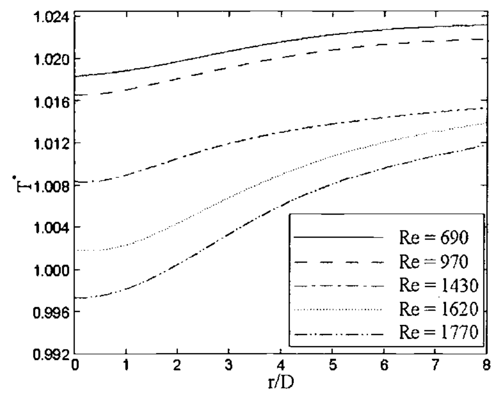

Fig. 3.6: Radial distribution of non-dimensional heated wall temperature for various Re at nozzle to surface spacing, H/D of 4.

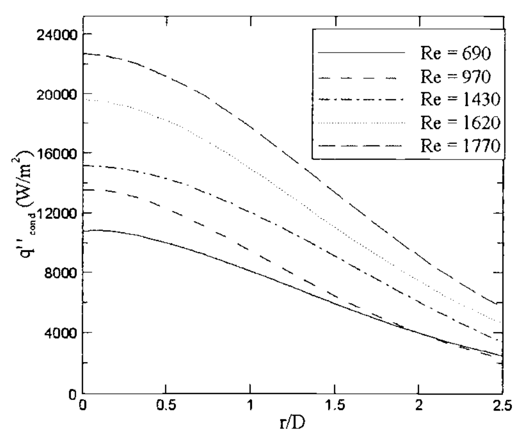

Fig. 3.7: Radial distribution of local conduction heat flux (q''_{cond}) for various Re at nozzle to surface spacing, H/D of 4.

3.7: UNCERTAINTY ANALYSIS

The uncertainties in measured variables are shown in Table 3.2. Precision error in temperature measurements was determined by analyzing 30 images at steady state for different Reynolds numbers. Bias error in measurements of r, H, I, T, T_{aw} and $\dot{Q}$ were obtained from manufacturer's specification. Pressure transducer and thermocouples were calibrated using a dead weight calibrator and a NIST traceable RTD respectively (Appendix A). The error in q''_{cond} was primarily due to error in estimating dT/dr. Uncertainty in temperature gradient was found by perturbing temperature data points and noticing the change in dT/dr for the best curve fit. Temperature data points were perturbed in different ways such as by varying temperature data from -0.28 °C at r = 0 to +0.28 °C at r = 6D linearly or in six equal steps. Note that 0.28 °C was the uncertainty in temperature measurement of the heated foil. The maximum error in dT/dr obtained from above procedure was used in performing the uncertainty analysis of other estimated variables. The errors in q''_{gen} and q''_{cond} were included to estimate the errors in Nu (Appendix B). The errors in estimated variables were calculated using propagation of errors method (Figliola and Beasley, 2000) and are shown in Table 3.3. The uncertainties are reported as absolute value or as percentage of the local value. To minimize uncertainties, original temperature data were used to make calculations in equations (3.1), (3.2) and (3.6) and curve fitting was performed only at last stage. Curve fit errors were also included in the uncertainty estimates.

Table 3.2: Uncertainties in measured variables

Variable	Bias error	Precision error	Total error
r	10 microns	--------	10 microns
H	7.5 microns	--------	7.5 microns
P_o	4.14 kPa (0.6 psi)	--------	0.6 psi
T_o	0.2 °C	--------	0.2 °C
T_{surr}	0.15 °C	--------	0.15 °C
I	1.8 %	--------	1.8 %
R_{foil}	1.5 %	--------	1.5 %
T	0.15 °C	0.23 °C (max)	0.28 °C
T_{aw}	0.15 °C	0.27 °C (max)	0.31 °C
$\dot{Q}$	10.4% (Re = 690) - 4% (Re = 1770)	--------	10.4% (Re = 690) - 4% (Re = 1770)

Table 3.3: Uncertainties in estimated variables

Variable	Error
Re	10.4%(Re = 690) - 4 %(Re = 1770)
Nu	8.1% (Re = 690) - 10.5 % (Re = 1770) at stagnation
T*	0.12% (max)
T^*_{aw}	0.14% (max)

3.8: RESULTS AND DISCUSSION

A nozzle of hydraulic diameter 500 μm was used to validate the experimental setup and procedure. Table 3.4 shows a comparison between the experimentally determined average Nusselt number, Nu_{av}, and that calculated using Martin's correlation (Martin, 1977) for a nozzle-to-surface spacing ratio, H/D of 2 and Re of 2024. The local data for this case is presented in Appendix G. The corresponding M was 0.185. The result indicates that the Nu_{av} values at all r/D locations varied by less than 10 percent from Martin's results. Henceforth, results for the 125-μm jet are presented.

Table 3.4: Comparison of Nu_{av} for a 500-μm- diameter jet impingement with Martin's correlation (H/D = 2; D = 500 μm; Re = 2024; V_{exit} = 64.34 m/s; M = 0.185)

R/D	Nu_{av} (Present study)	Nu_{av} [1]
2.5	21.93	23.82
3.0	20.48	21.76
3.5	19.36	19.76
4.0	18.31	18.00

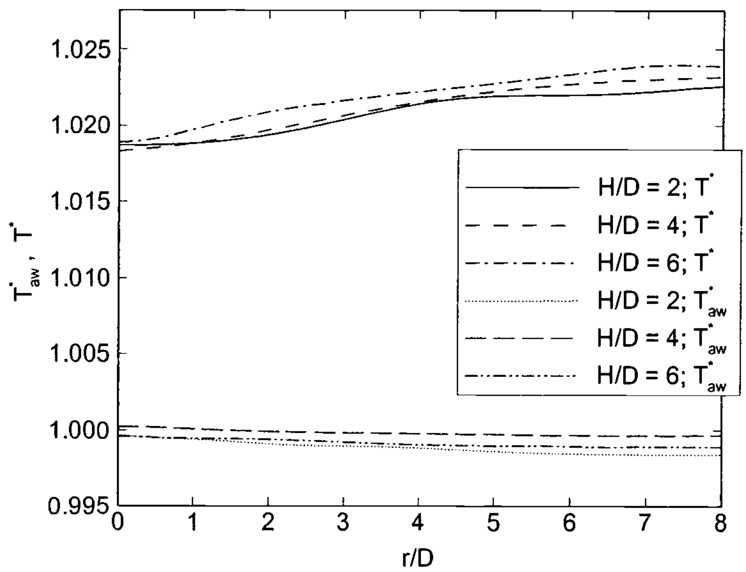

Fig. 3.8: Non-dimensional adiabatic and heated wall temperature distribution for Re = 690

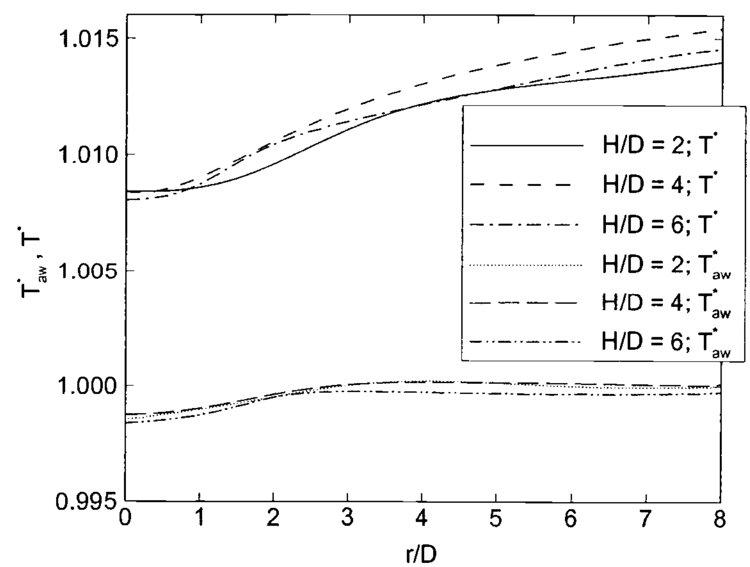

Fig. 3.9: Non-dimensional adiabatic and heated wall temperature distribution for Re = 1430

Figures 3.8 and 3.9 shows radial distribution of non-dimensional adiabatic and heated surface temperature profiles for Re = 690 and 1430 for three spacings of H/D = 2, 4, and 6. In present experiments, a jet with Re = 690 is incompressible and that with Re = 1430 is compressible. The trends observed in these figures are typical of those for the other Re studied (Appendix C). The surface temperatures were normalized with the stagnation temperature of the jet. The plots indicate that the microscale jet is fairly insensitive to H/D variation. This is consistent with the numerical results of Pence et al. (2003), but contrary to observations made by Goldstein et al. (1986) in their study of macroscale incompressible turbulent jet impingement. They observed a distinct rise in recovery factor, R, with an increase in H/D at radial locations of r/D = 0 and 2. The first radial location corresponded to the stagnation point while the second corresponded to a location where the radial profile of R exhibited a minimum for all H/D $\leq$ 4. The rise in R at the stagnation point was attributed to the entrainment of warmer ambient air into jet flow. A low recovery factor at r/D = 2 for H/D $\leq$ 4 was attributed to the presence of vortices in the outer shear layer of the jet flow past impingement. A breakdown of these vortices with increasing H/D caused a rise in R at this location.

The relative insensitivity of surface temperature to H/D observed in Fig. 3.8 and 3.9 can be attributed to reduced entrainment of the low Re microscale jet compared to macroscale turbulent jets. The low Re suggests laminar flow at the jet exit. However, it is well known that a laminar free jet undergoes a transition to turbulence at some distance downstream of the nozzle exit. Based on a classification provided by Viskanta (1993), a free jet can be considered fully laminar between $300 < \mathrm{Re} < 1000$, and transitional between $1000 < \mathrm{Re} < 3000$. Although the results of free jets are not directly applicable to impinging jets, a single impinging jet can be considered laminar up to a Re = 2,500 (Viskanta, 1993). It is unclear whether this criterion can be used regardless of the H/D spacing.

Page and Hill (1966) proposed a limit for the extent of the transition region for free jets with a laminar exit velocity. They suggested that the jet transitions to turbulence at a Re based on jet length, $\mathrm{Re}_H \approx 100$ and becomes fully turbulent at a $\mathrm{Re}_H \approx 10^6$. In the case of microscale jets, high velocities ensure that transition to turbulence begins at a short distance from the nozzle exit; while the nozzle-to-surface spacing ratio at which the jet becomes fully turbulent is large. Previous studies have also shown that the influence of the impingement surface on the mean flow and turbulence of the oncoming free jet extends to less than two nozzle diameters upstream of the surface (Donaldson et al., 1971). Hence it can be reasoned that the microscale jet is in the early stages of the transition prior to impingement for all spacings and Re examined in this study. Henceforth, all the results are presented for a fixed spacing of H/D = 4.

Figure 3.10 presents profiles of the radial distribution of the non-dimensional adiabatic wall temperature in terms of the R plotted for five M corresponding to Re varied during the experiments. The plots show a distinct reduction in R around the stagnation region with increasing M. This trend is consistent with the adiabatic wall temperature profiles presented by Pence et al. (2003) for microscale jets, but contrary to the observations of Goldstein et al. (1986) for an incompressible, turbulent macroscale jet. Goldstein et al. (1986) found that R was insensitive to Re variation for H/D between 2 and 12. The observed changes in the R profile for different Re in the present study is attributed to fluid compressibility effects of the microscale jet flow. Meola et al. (1995) performed experiments on high Re (turbulent), compressible, circular air jet impingement. They mapped the temperature distribution on the surface of a thin foil using IR scanning thermography, and observed a minimum in R at $r/D \approx 1.6$ for jet impingement at $H/D = 4$ and $M = 0.41$. At the stagnation point, they observed a trend similar to Goldstein et al. (1986) with an increase in H/D. At $M > 0.7$, azimuthal flow instabilities were observed surrounding the stagnation point. These instabilities resulted in two minima in R with r/D for all H/D. At $H/D > 6$, the flow instability was observed at a much lower M of 0.41. In the present study, no such flow instability was observed within the range of M and H/D studied. The apparent contradiction could be a result of the different flow regime associated with a low Re and high M jet impingement in the present experiments.

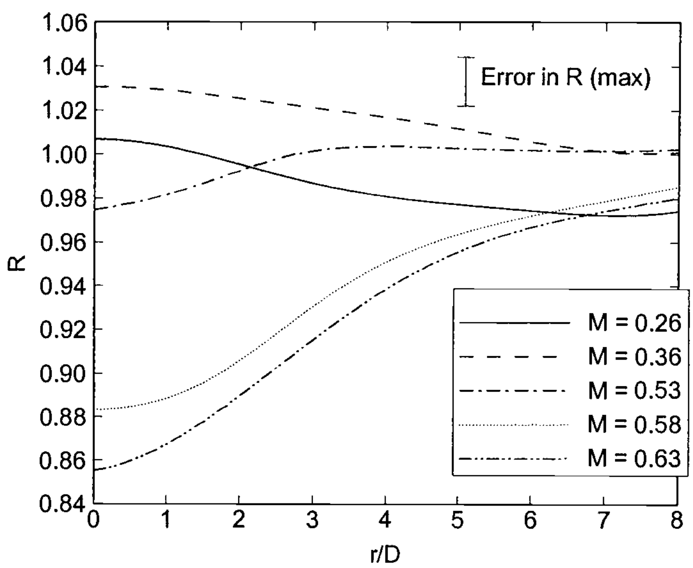

Fig. 3.10: Radial distribution of recovery factor along the wall for H/D = 4.

Figure 3.10 shows a small rise in recovery factor for M = 0.36 after which the recovery factor decreased with an increase in M. This rise was consistently observed at all spacings which could be a result of the small heat transfer that occurs from the surroundings to the cooler fluid flowing in the microtube nozzle. However, no definite conclusions can be stated since the increase was within the uncertainty in R.

Theoretically, for a compressible flow the recovery factor is unity ($T_{aw} = T_o$) at the stagnation point and is a minimum where the hydrodynamic boundary layer is thinnest. For circular compressible microscale jets with a uniform velocity profile, Pence et al. (2003) determined that for a M of 0.6, the location of this minimum occurred at approximately r/D = 0.75. In wall-bounded compressible flows, R is less than unity due to the heat conduction that occurs in the thin fluid boundary layer

(Shapiro, 1985; Kays and Crawford, 1993). The heat conduction rate increases with an increase in M and with a decrease in boundary layer thickness. While a reduction of R with increasing M seen in Fig. 3.10 is consistent with theory, the location of the minimum at the stagnation point (as opposed to r/D $\approx$ 0.75) is not. The observed low R at the stagnation point can be attributed to lateral foil conduction that resulted from the small length scales and moderate thermal conductivity of the foil. A radial location of r/D = 0.75 for M = 0.63 corresponded to a radial distance of 94 μm, across which a temperature differential of approximately 3 °C had to be sustained. This corresponded to a large temperature gradient of approximately 32,000 °C/m, which, given the finite thermal conductivity of the inconel foil, resulted in a large lateral foil heat conduction away from the stagnation point. This caused a bleeding of the low temperature region into the stagnation point, thereby lowering the temperature from the theoretical T_o. It is interesting to note that a R < 1 at the stagnation point can also be observed in the graphs presented in Meola et al.(1995) for H/D < 7. One way to limit the temperature distortion effect in microscale jet impingement is to select a very low thermal conductivity foil. However, such materials also tend to have a very high specific resistivity which would entail the use of a power supply with a high load capacity. Since the present measurements cannot be used to determine the location of the true minimum in R, an estimate can be obtained by invoking studies in the literature. The location of the highest shear region is sensitive to the exit velocity profile, Re, and H/D. As mentioned previously, Pence et al. (2003) observed a minimum in T_{aw} around r/D = 0.75 for a M = 0.6 laminar jet with a uniform exit profile and cosine-tapered ends. Chatterjee and Deviprasad (2001) performed a numerical study to investigate the effect of upstream diffusion for confined laminar jet impingement with a parabolic exit profile. For $H/D < 1$, they suggested that vorticity generated near the impingement surface diffused upstream and distorted the streamwise mean velocity jet exit profile from its original parabolic shape to a more uniform one. The jet exit profile remained undistorted for a $Re > 100$ and $H/D > 1$, since forced convection suppressed upstream vorticity diffusion. In the present experiments, the lower bound on Re and H/D are 690 and 2 respectively, which, based on Chatterjee and Deviprasad's results (2001), would preclude any distortion of the exit velocity profile due to vorticity diffusion.

Saad et al. (1977) performed a computational study on incompressible laminar jets with parabolic and uniform jet exit velocity profiles. Their study showed that the stagnation point Nu and peak non-dimensional skin friction (C_f) were greater for parabolic profile than for the uniform velocity profile under identical Re and nozzle spacing. The non-dimensional skin friction, C_f, peaked at a radial distance r/D of 0.4 for a parabolic velocity profile corresponding to the location of the highest shear. In contrast, C_f peaked at r/D of 0.6 for the uniform exit velocity profile jet. Based on the results of Saad et al. (1977), it is reasonable to expect that the location of minimum R in the present experiments would occur closer to the stagnation point than predicted by Pence et al (2003). Note, however, that the minimum would not occur at exactly $r/D = 0.4$ since a slip-velocity boundary condition may be warranted (Pence et al., 2003) for microscale jets.

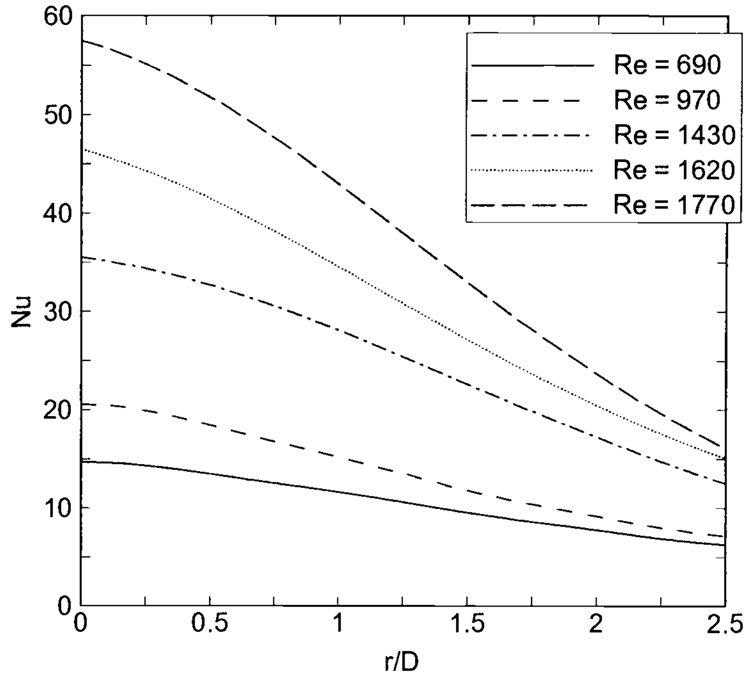

Fig. 3.11: Radial distribution of local Nusselt number for H/D = 4.

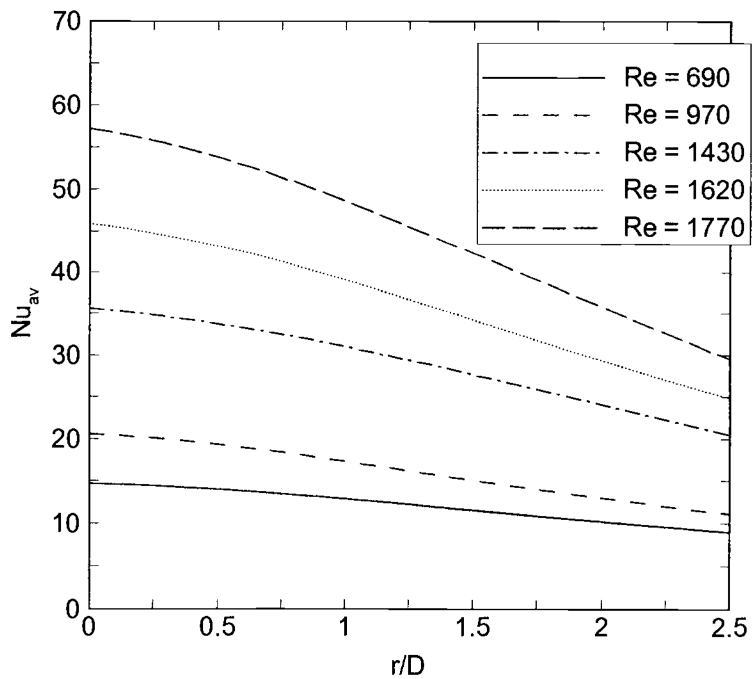

Fig. 3.12: Radial distribution of average Nusselt number for H/D = 4.

The local and average Nu distributions for various Re are presented in Fig. 3.11 and 3.12. The plots show a monotonically decreasing trend for Nu with r/D. The reported values are significantly larger than that observed by Pence et al. (2003), especially at high Re. For an incompressible laminar jet, Saad et al. (1977) have shown, that the local Stanton numbers near the stagnation region for a parabolic profile are larger than those for a uniform profile and follow a monotonically decreasing trend with r/D. Thus, the Nu trend in Fig. 3.11 is consistent with the trends observed for a parabolic exit velocity profile. Another consequence of the parabolic velocity profile is a thinner developing boundary layer flow near stagnation point, which results in a larger Knudsen number based on boundary layer thickness than that speculated by Pence et al. (2003). This could provide a correspondingly larger slip velocity and temperature jump, thereby providing a further enhancement in heat transfer rates compared to their study.

The experimentally determined Nu_{av} were compared with Martin's correlation (1977) at an r/D = 2.5, and are tabulated in Table 3.5. Note that Martin's correlation is valid for $2{,}000 \le Re \le 400{,}000$; $2 \le H/D \le 12$; and $2.5 \le r/D \le 7.5$ and is given by

$$\left(\frac{Nu_{ave}}{Pr^{0.42}}\right)=\frac{D}{r}\cdot\frac{1-1.1D/r}{1+0.1(H/D-6)D/r}F(Re) \tag{3.9}$$

Here the function F(Re) is given by

$$F(Re)=2Re^{1/2}\left(1+\frac{Re^{0.55}}{200}\right)^{0.5} \tag{3.10}$$

The maximum Re in the present experiments of 1770 is outside the range of this correlation. The present Nu_{av} values are higher for higher Re and lower for lower Re compared to Martin's correlation. The higher Nu_{av} for higher Re can be attributed to compressibility effect, which increases the density of air in the impingement region and hence the heat transfer rates and a possible slip flow regime along the impingement wall (Pence et al, 2003; Kreith et al, 2000). The reason for the large deviation from Martin's correlation for the low Re cases cannot be explained solely by experimental uncertainties (see Table 3.3), and warrants further investigation.

Table 3.5: Comparison of results obtained in present study with that obtained using Martin's correlation at an r/D = 2.5.

	Nu_{av} (Martin's correlation)			Nu_{av} (Present study)
Re	H/D = 2	H/D = 4	H/D = 6	H/D = 4
690	15.23	13.91	12.79	9
970	18.34	16.75	15.41	11.1
1430	22.75	20.77	19.11	20.5
1620	24.39	22.27	20.49	24.8
1770	25.64	23.41	21.54	29.5

3.9: CONCLUSIONS

Microscale axisymmetric jet impingement heat transfer was studied experimentally using microscopic IR thermography. The jet flow was confined and submerged, and issued from a nozzle with a cross-sectional diameter of 125 μm. Experiments were performed for 5 Re between 690 and 1770 (corresponding M ranged between 0.26 and 0.63) for three H/D ratios of 2, 4 and 6. The salient conclusions drawn from the experiments are listed below.

1. An experimental and data analysis procedure is outlined.
2. Lateral conduction along the foil is found to be significant for microscale flows because of the small length scales and should be included in the calculation of heat transfer rates.
3. Microscale jets are insensitive to H/D variation within the range of experiments.
4. The recovery factor for microscale jets is less than unity near stagnation point region and decreases with an increase in Re.
5. Azimuthal instabilities that are observed around the stagnation point in high subsonic M turbulent impinging jets (Meola et al, 1995) were not seen for the microscale jet.
6. Average Nu obtained in this study are significantly higher for higher Re compared to predictions using Martin's correlation (Martin, 1977). This was attributed to fluid compressibility and a possible slip flow regime along the impingement wall.

CHAPTER 4: MICROSCALE INTERNAL FLOW

4.1: INTRODUCTION

Ever since Tuckerman and Pease (1981) demonstrated the enhanced heat transfer capabilities of a single phase microchannel heat sink with uniform channel cross-section, many studies of single and more recently, two-phase flow and heat transfer in microchannels have been reported. Recent review papers (Palm, 2001; Ghiaasiaan and Abdel-Khalik, 2001; Kandilkar, 2002; Hassan et al., 2004) have summarized various experimental and modeling efforts in this field.

Measurement of local surface temperatures is important in order to determine the heat transfer in microchannel flows. Palm (2001) summarized that heat transfer results of various single phase flow studies were contradictory, with both high and low Nu reported for laminar flows. He attributed these discrepancies to the difficulties in measurement of fluid and surface temperatures in microchannels. In the study of two phase heat transfer, Jiang et al. (2001) highlighted a need for direct measurement of channel wall temperatures to permit generation of reliable boiling curves.

Typically, surface temperature measurements are performed either using thermocouples located at some depth below the wall-fluid interface of the microchannel (for example, Qu et al., 2003; Peng et al., 1994; Tso et al., 2000), or by a few thin-film resistance temperature detectors deposited directly on the bottom side of silicon (Si) heat sink (for example, Jiang et al., 2001; Koo et al., 2001; Zhang et al., 2002; Popescu et al., 2002). Interpreting local heat transfer results using the above method has some ambiguity due to lateral (axial) conduction along the highly conductive metallic or Si walls. The Si heat sinks with integrated sensors also have associated fabrication complexity and cost. Besides, the temperature measurements are typically restricted to a few local points along the channel walls.

Recently, there have been some studies on non-intrusive imaging of the heat sink or heater surface temperatures in microchannels. Hestroni et al. (2001, 2003) performed visualization studies of flow boiling in triangular cross-section microchannel arrays for two different plenum designs using high speed imaging (recorded at 1000 frames/second) for flow visualization and IR radiometry of the heater surface. They reported irregularities in spanwise heater surface temperatures due to flow instabilities under uniform and non-uniform heat flux conditions. Hollingworth (2004) measured the local channel wall temperature distribution in single and two-phase minichannel flows using thermochromic liquid crystal imaging of heated side wall. The three other side walls were adiabatic. Most of the data presented were for flows in the turbulent or transitional regime, and agreed well with correlations in the literature. Hapke et al. (2002) used IR thermography to examine the outside wall temperature distribution for flow boiling in rectangular microchannels and concluded that it is possible to detect axial position of the different boiling regions using this technique. Hohmann et al. (2002) applied the uncapsulated thermochromic liquid crystal technique to perform a high spatial resolution (~1 μm) temperature measurement in an evaporating liquid meniscus problem. Buffone and Sefiane (2004) applied IR thermography to map temperature along the interface of an evaporating meniscus in capillary tube.

Fletcher et al. (2003) demonstrated a near-field method for improving the spatial resolution (< 5 μm) of infrared camera by using a microfabricated Silicon solid immersion lens. The infrared radiation was collected by solid immersion lens and measured using a conventional infrared microscope. The lens was mounted on a cantilever beam that scanned the sample surface. Their imaging approach improved the edge response of the IR camera by a factor of four and was able to resolve differences in metal lines separated by 4 μm.

Significant advances have also been made in nano-scale temperature measurement using a near-field optical microscopy technique (Goodson et al., 1997). This technique provides excellent spatial resolution on the order of 50 nm, but requires that the fiber optic probe be located very close to the surface, and has consequently not been used for microchannel wall temperature measurements. Typically, such high spatial resolutions may not be needed for temperature measurement in channels with dimensions ranging from tens to hundreds of microns.

4.2: NOMENCLATURE

a	Absorption coefficient (cm^{-1})	Pr	Prandtl number ($Pr = c_p \cdot \mu/k$)
$\overline{A}$	Total absorption	q"	Heat flux to the channel walls (W/m^2)
c_p	Specific heat (J/kg-K)		
D_h	Channel hydraulic diameter (m)	Re	Reynolds number ($Re = V \cdot D_h / \nu$)
E	Emitted energy flux $E = \varepsilon\sigma T^4 = \varepsilon E_b (W/m^2)$	$\overline{R}$	Total reflection
		S	Radiation path length (m)
G	Incident energy flux (W/m^2)	t	thickness of the medium (cm)
h	Convective heat transfer coefficient (W/m^2-K)	$T_{b,i}$	Bulk fluid temperature at position 'i' (°C)
H	Height of the channel (m)	$T_{b,in}$	Inlet bulk fluid temperature (°C)
i	Total energy flux (W/m^2)	$T_{b,ex}$	Exit bulk fluid temperature (°C)
k	Fluid thermal conductivity (W/m-K)	T_s	Temperature of the heat sink top surface (°C)
L	Channel length (m)	T_w	Fluid top interface temperature (°C)
$\dot{m}$	Mass flow rate (kg/s)		
n	Refractive index	T_{sur}	Surrounding temperature (°C)
Nu	Nusselt number ($Nu = hD_h/k$)	$\overline{T}$	Total transmission
P	Perimeter of channel (m)	W	Width of the channel (m)
Pe	Peclet number (Pe = Re.Pr)	x_i	Distance of position 'i' from the

	channel entrance (m)
x^*	Non-dimensional axial distance ($x^* = x/(D_h \cdot Pe)$)

Greek Symbols

α	Absorptivity
ε	Emissivity
λ	Wavelength
μ	Dynamic viscosity of fluid (Pa·s)
ν	Kinematic viscosity of fluid (m^2/s)

Superscripts and subscripts

bl	Blackbody
det	Detector
f	Fluid
hs	Heater surface
lens	Camera lens
Si	Silicon

4.3: OBJECTIVES AND JUSTIFICATION

Visualization and local heat transfer studies discussed previously have used channel walls with three sides fabricated of one material and the fourth side of a different optically clear material. For example channels etched in silicon use an anodically bonded glass top surface for flow visualization and measurement. This complicates interpretation of global measurements that are typically performed in channels with walls made of opaque (to visible light) high thermal conductivity materials. Differences could arise between visualization and global measurement due to the nature of heat flux distribution peripherally and axially for single phase flows, and to peripheral differences in contact angle and heterogeneous nucleation site location for flow boiling. Such concerns have prompted recent interest in the development of IR particle image velocimetry technique (Chung et al., 2001; Han et al., 2004; Liu et al., 2004) for quantitative flow visualization in all-Si heat sinks. However, quantitative local heat transfer measurements in such microchannels have, as yet, to be addressed.

The study presented here is unique in that direct measurements of detailed channel wall, or near-wall fluid, temperature in an all-Si side wall microchannel is presented. Inconsistencies in interpretation of local imaging and global measurements mentioned above can be avoided using this technique. Direct measurement of the local fluid temperature near the inner wall of a microchannel provides an accurate estimate of the local heat transfer variation along the channel.

Data of single phase laminar water flows over a limited inlet Re range of 200 to 300 (Pe = 770 to 1370) are presented for a single rectangular microchannel of width 50 μm and depth 135 μm (Appendix F). The working fluid used was deionized water. Experiments were performed at four different flow rates and a fixed heater electrical power. The entire test section was heated using a thick-film heater that distributes heat over the heat sink.

4.4: RADIATION THEORY

In order to use IR thermography, it is important to isolate the energy irradiated by the object of interest. This becomes a challenge in microchannel flows, and requires a careful estimation of radiant energy contributions and calibration. This section summarizes net radiant energy flux estimation in a rectangular closed channel flow for an IR-opaque fluid/channel wall based on classical radiation theory (Siegel and Howell, 2002). For an IR-opaque fluid and transparent channel walls, μ–IRT can provide the temperature of the fluid in contact with the upper channel wall, or, the channel wall surface temperature for the case of an IR-opaque channel wall. In both cases, the heat sink is assumed to be fabricated using a material that is IR-transmissive. Several key assumptions made in the radiation analysis are listed below.

1. The IR camera captures normal radiaiton emitted from the target object. Hence, the path length through Si and water is considered equal to their thickness for following analysis.
2. 135 μm deep water column is opaque to radiaiton in detector wavelength range. The Planck mean absorption coefficient $a_{f,Planck}$ for water in the detector range was found to be equal to 319 cm^{-1} (at 40 °C). The transmissivity of 135 μm deep water will be given by

$$\tau_f = \exp\left(-a_{f,Planck} \cdot t_f\right) \approx 0 \tag{4.1}$$

Thus the water opacity assumption is appropriate for the detector range.

3. The detector temperature, T_{det}, is known.

4. The detector lens and body are at a known ambient temperature, $T_{lens} = T_{sur}$.
5. The Water surface is a diffuse emitter.
6. All properties are known *a prior* or can be estimated by calibration.
7. Air between the heat sink and the detector is non-participating medium in radiation exchange. This is true since the distance between the camera optics and the target test section is small (< 30 mm) and because there are narrow band filters in front of the detectors to filter atmospheric CO_2 and H_2O gas emissions.
8. Losses/corrections for stray unfocussed radiation incident on the detector array from the camera internals are calibrated by the manufacturer and mostly eliminated by careful design. Such radiation effects can be included and estimated by another intensity term (Horny, 2003), but have not been included in this analysis.

Figure 4.1 shows a schematic of the microchannel with the various radiant energy terms that need to be accounted for water flow in microchannels. In general, each pixel (sensor) will have varied contributions due to each of these fluxes depending on their (x,y) location in the array. For example, the detectors located at the periphery of the array will be detecting largely intensity emanating from the heater surface through the Si test device. For the rest of the analysis, the (x,y) dependence is implicitly understood.

The total radiation energy flux incident on pixels (x,y) of the detector array focused on near wall fluid region mainly consists of radiation emitted by water, radiation emitted by channel Si wafer and detector reflection reflected from top Si wafer, and is given by

$$i_{det} = \overline{T}\left(\varepsilon_f E_{bl,f}\right) + \varepsilon_{Si} E_{bl,Si} + \overline{R}(G_{det}) \tag{4.2}$$

Here, the reflected surroundings radiation flux is neglected as the configuration factor from surroundings to the target was close to zero.

In order to estimate the true temperature of the near-wall water from the net intensity detected by the camera, the following radiative quantities and properties are needed:

The transmittance of 215 μm thick Si wall on detector side, neglecting scattering, can be given by

$$\tau_{Si} = \exp\left(-a_{Si} t_{Si}\right) \tag{4.3}$$

Using the bulk absorption coefficient of Si (Hordvik et al., 1977) as $4.2\text{x}10^{-4}$ cm^{-1} (at 3.8 μm) in Eq. 4.3 gives τ_{Si} nearly equal to one. The above result gives absorbance and hence the emittance of channel Si wafer to be equal to zero. This in turn implies that the radiation emitted by Si is negligible and hence the second term in Eq. (4.2) can be neglected. Since the detector is cryogenically cooled to a temperature of 77 ^{o}K, the detector radiation reflected from top Si wafer is negligible. Thus the radiation reaching detector is primarily emitted from near wall water region and hence this technique will give temperature of water close to wall.

Since τ_{Si} is nearly equal to one, the total reflected radiation incident from air and water side on the channel Si wafer will be equal and is given by

$$\overline{R} = \frac{\rho_{Si-A} + \rho_{Si-f} - 2.\rho_{Si-A} \cdot \rho_{Si-f}}{1 - \rho_{Si-A} \cdot \rho_{Si-f}} \tag{4.4}$$

As the extinction coefficient for air, water and Si is negligible in detector IR range, the surface reflectivity at their interfaces can be evaluated by

$$\rho_{1-2} = \left(\frac{n_1 - n_2}{n_1 + n_2} \right)^2 \tag{4.5}$$

Here n_1 and n_2 are the refractive indices of the mediums 1 and 2 forming an interface.

The radiation emitted by water in a Si medium is given by

$$E_f = n_{Si}^2 . \varepsilon_f . \sigma . T_f^4 \tag{4.6}$$

The Si transmittance to radiation emitted by water at the water-Si interface can be evaluated by

$$\overline{T} = 1 - (\overline{R} - \rho_{Si-f}) \tag{4.7}$$

The water radiation reaching detector is given by

$$i_{det} = \left(\frac{1}{n_{Si}^2} \right) . \overline{T} . E_f = \left(\overline{T} . \varepsilon_f \right) \sigma . T_W^4 \tag{4.8}$$

The refractive indices of air, water and Si in range 3.5 – 5.1 mm are 1 (Siegel and Howell, 2002), 3.43 (Edwards and Ochoa, 1980) and 1.4 (Bertie and Lan, 1996) respectively. This values gives $\overline{R}$ of 0.39 and $\overline{T}$ equal to 0.79.

The uncertainty in estimating T_W is primarily due to the errors in estimating $\overline{T}$ and ε_f. Using Eq. (4.8) and propagation of error technique, the uncertainty in temperature measurement due to error in estimating $\overline{T}$ and ε_f is given by

$$\frac{u_{T_W}}{T_W} = \frac{1}{4}\sqrt{\left(\frac{u_{\varepsilon_f}}{\varepsilon_f}\right)^2 + \left(\frac{u_{\overline{T}}}{\overline{T}}\right)^2} \tag{4.9}$$

Note that T_w in the above equation is in degree Kelvin. Equation 4.9 shows that the absolute uncertainty in temperature measurement can be reduced for the present technique by reducing u_{ε_f} and $u_{\overline{T}}$ and increasing $\overline{T}$ and ε_f. The former was achieved by performing a detailed onsite calibration to estimate the combined $\left(\varepsilon_f \overline{T}\right)$ factor for the current setup and the latter was attained by coating the top side of the channel wafer by an antireflection coating, thereby increasing the ρ_{Si-A} and hence $\overline{T}$ to about 0.98. Note that water has a high emissivity, approximately 0.98, which aids in the application of this technique.

The fraction of radiation transmitted through an absorbing-scattering medium depends on the spectral variation of the extinction coefficient of the medium and the radiation path length (Siegel and Howell, 2002). Neglecting scattering, Bouger's law gives the net attenuation of radiation through an absorbing medium to be

$$\frac{i_\lambda(S)}{i_\lambda(0)} = \exp\left[-\int_0^S a_\lambda(y)dy\right] \tag{4.10}$$

In order to provide an estimate of the depth average of estimated water temperature by the detector, the attenuation of water radiating to the top channel surface was estimated using Eq. 4.10. The Absorption coefficient for water in the wavelength range of the detector (Siegel and Howell, 2002) varies from a high of 721 cm^{-1} at 3.4 μm to a low of 112 cm^{-1} at 3.8 μm. Calculations were performed by treating a_λ to be independent of path length to estimate the optical thickness of water. An optical path length of 72 μm resulted from using a Plank mean absorption coefficient of 319 cm^{-1} over the detector wavelength range. Although these values may seem large, it is important to note that the intensity attenuation is exponential, and that the sensitivity of radiation incident on the detector to radiation at such depths is small. A large portion of radiated energy from water will be restricted to a region of a few microns thick near the channel upper wall. In this sense, the temperature represents an average fluid temperature in the near-wall region.

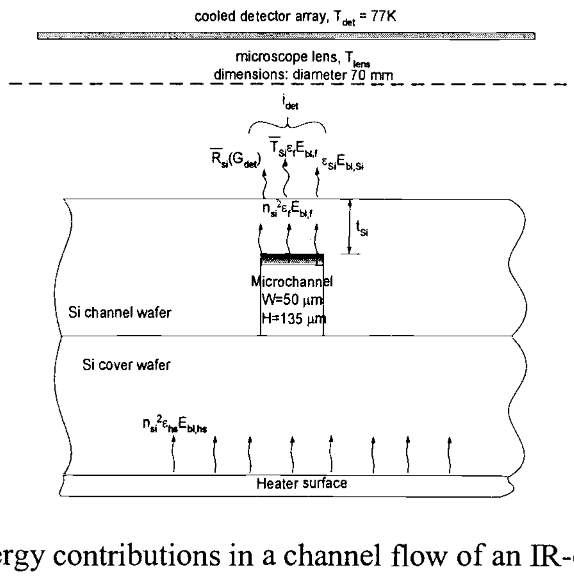

Fig. 4.1: Radiant energy contributions in a channel flow of an IR-opaque fluid.

4.5: EXPERIMENTAL FACILITY

Figure 4.2 shows a schematic of the open-loop experimental facility. A constant flow rate of water through the system was generated using pressurized air. Filtered, compressed air was supplied through a settling tank to the pressurized water tank by a dedicated compressor. The pressure in the reservoir was regulated by the pressure reducing value located downstream of the settling tank. The water flow rate was controlled by a micrometer needle valve and measured by a Coriolis flow meter (Micro Motion Inc., Sensor CMF010 with 2700 transmitter). Differential pressure between the microchannel inlet and atmosphere, and water temperature prior to the plenum were measured using a capacitance-type pressure transducer (Validyne, Inc., DP45 with CD15 modulator/ demodulator) and a calibrated K-type thermocouple, respectively.

The test section schematic is shown in Fig. 4.3. It consists of a Si heat sink that encloses a single 50 μm wide by 135 μm deep rectangular microchannel of length 13 mm. The side and bottom channel walls were fabricated onto a 350 μm channel wafer using a deep reactive ion etching (DRIE) technique. The fourth channel wall was formed by a second 350 μm cover wafer that was anodically bonded to the channel Si wafer. Fluid entered the channel through a nanoport fitting into a 2-mm-diameter inlet plenum that was laser drilled into the cover wafer at Oregon State University. The DRIE and diffusion bonding were performed by an external vendor. The heat sink was inverted for IR visualization such that the water flow was visualized through the channel wafer. To minimize uncertainty in temperature measurement, a broad band anti-reflective (AR) coating in the wavelength range of 3 to 5 μm was deposited on the wafer. The vendor claims a total transmissivity for Si wafer in air of around 0.97 with this coating. Preliminary onsite calibration experiments confirmed this claim.

The Si heat sink was heated from the cover wafer side by a 5-mm long, 12-mm wide thick-film Kapton heater. The heater was located approximately 2 mm away from the channel exit. A 25-μm-thick copper foil, covering the area of heat sink past the plenum, was placed between the heater and the Si heat sink. The heater was attached to the copper foil by means of thermally conductive double-sided tape. The heat sink was firmly located above the copper foil and heater using adhesive tape around the periphery of the heat sink onto a thermal insulated Teflon™ base and by a U- shaped plexiglass clamp. The placement of a low emissivity material (such as the copper foil in this case) below the microchannel in between the heat sink and heater was critical in avoiding degradation of the detector sensitivity to water temperature caused due to large emission from the bottom and surrounding high-emissivity surfaces, such as the double-sided tape or thick-film heater.

Water exited the channel into an exit chamber (see Fig. 4.3) cut into the test section Teflon™ base. Because a jet was formed for most of the flow conditions tested, a foil deflector was located in the chamber to direct the jet into the exit chamber.

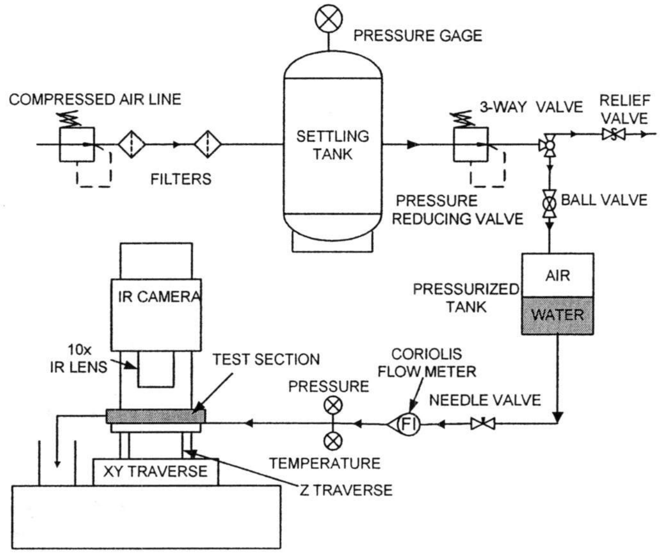

Fig. 4.2: Schematic of test apparatus

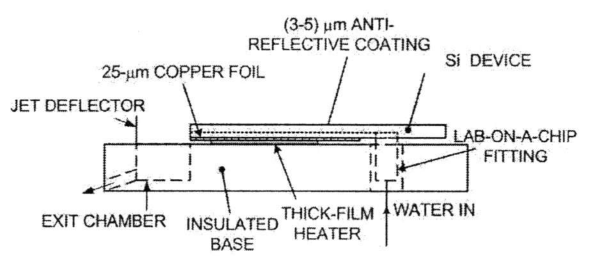

Fig. 4.3: Test section schematic

4.6: EXPERIMENTAL PROCEDURE

a) Calibration: The IR radiometer primarily detects intensity emitted by water that is transmitted through the top Si wall. An in-situ calibration was performed to determine the combined water emissivity and Si transmissivity factor as a function of location along the channel. Water at 23.5 ^{o}C was pumped through the microchannel and intensity maps were recorded at 14 different locations along the channel. These maps were used to determine the combined local emissivity-transmissivity correction factor at each location. An average of 10 intensity maps recorded at 30 frames per second was used to determine local correction factors.

b) Temperature measurement procedure: During test conditions the Kapton® heater located below the Si channel was used to deliver constant electric power of 2.31 W to the heat sink. The electrical energy input was determined using voltage and current measured at the power supply. This value of power ensured a minimum rise of 10 ^{o}C in bulk fluid temperature along the total length of the channel for all test conditions. Overlapping intensity maps that each covered 2.54 mm of axial channel length were recorded at 14 locations spaced 1 mm apart. Care was taken to ensure identical micrometer traverse location between the calibration and test conditions. Inlet bulk fluid temperature was based on IR measurement at the entrance to the microchannel, while the exit bulk temperature was directly measured using a calibrated thermocouple located approximately 2 mm from the exit. The above procedure applied to a typical IR image is shown in A`ppendix E.

A separate set of experiments was also performed to determine the top surface temperature of the heat sink directly above the microchannel. This was accomplished by coating the top surface with flat black paint and performing IR thermography on that surface at same test conditions. The procedure used to obtain the T_s measurements was similar to that used to obtain near-wall water temperatures.

4.7: DATA ANALYSIS

Average intensity maps were computed as mentioned in the previous section at each of the 14 axial locations. These maps were corrected for water emissivity and Si transmissivity to determine true temperature data along the length of the channel. Figure 4.4 shows a typical true T_w composite obtained from raw temperature images at the 14 locations for Re = 297 test condition. The true temperature data obtained from location adjacent to each other have overlapping regions where the data were averaged to obtain a final T_w value for that position. The averaged temperature data thus obtained were curve fitted using Tablecurve 2D® software. Note that all the data points are not plotted to retain clarity of the figure.

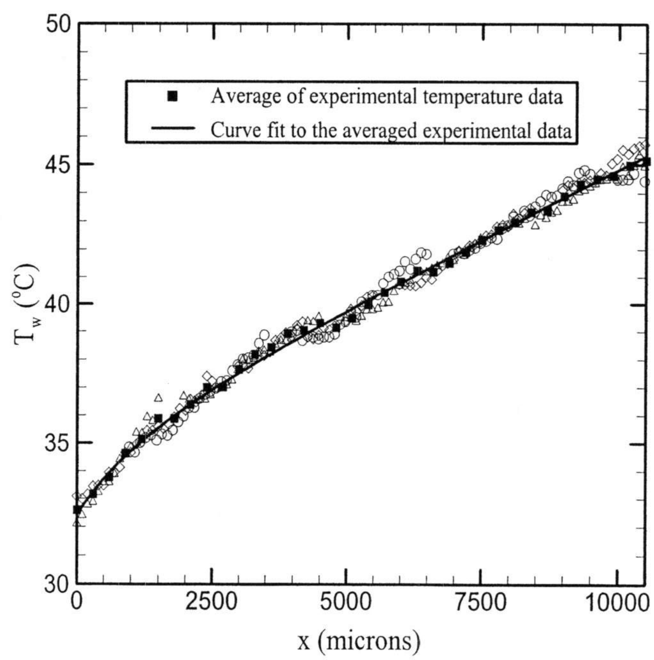

Fig. 4.4: Data analysis procedure to determine near-wall fluid temperature, T_w, distribution from IR image files; Re = 297; $q'' = 18.87$ W/cm^2. The unfilled symbols represent true temperature data.

Two cases of heat transfer were calculated. In the first case, the channel heat flux was assumed to be uniform axially and was calculated by

$$q'' = \frac{\dot{m} c_p (T_{b,ex} - T_{b,in})}{PL} \tag{4.11}$$

The bulk fluid temperature will vary linearly in this case from the inlet to the exit of the channel. This method of estimating q'' is more direct and has lesser uncertainty than that based on using electric heat input because of the difficulty in accounting for heat losses accurately.

The local heat transfer coefficient and Nusselt number (Nu) along the length of the channel for this constant heat flux case was estimated, respectively, using

$$h_i = \frac{q''}{(T_{w,i} - T_{b,i})} \tag{4.12}$$

$$\text{and } Nu_i = \frac{h_i D_h}{k} \tag{4.13}$$

In the second case the channel heat flux was modeled to vary axially to account for the axial conduction effects. This was done using the difference between the top surface temperature and near wall fluid temperature as weights to distribute the channel heat flux axially. Note that this method was used to provide approximate estimate of variation in heat flux along the channel length and does not have a theoretical basis. The local temperature gradient and Fourier's law of conduction could have been used to directly calculate the local heat flux from the top wall. However, this results in high uncertainty in heat flux estimation due to the small length scale and high thermal conductivity of Si. The local heat flux at each pixel position, 10 μm apart, was calculated using

$$q''_{var,i} = \frac{\dot{m}c_P(T_{b,ex} - T_{b,in})}{P(x_{i+1} - x_i)} \left(\frac{(T_{s,i} - T_{w,i})}{\sum_{i=1}^{N}(T_{s,i} - T_{w.i})} \right) \tag{4.14}$$

The local bulk fluid temperature for axially varying boundary condition was calculated using

$$T_{b,i} = T_{b,i-1} + \frac{q''_{var,i-1}}{\dot{m}c_P} \tag{4.15}$$

The local heat transfer coefficient and Nu for this case were determined respectively using Eqs. 4.12 and 4.13.

4.8: UNCERTAINTY ANALYSIS

Uncertainties in measured and estimated variables are shown in Table 4.1. The precision error in temperature measurement was determined by analyzing 10 images at steady state for different Reynolds numbers. The bias error of the IR camera, curve fit error and the uncertainty in estimating correction factor, $\left(\varepsilon_f \overline{T}\right)$ were included in the uncertainty analysis (Appendix D). Bias error in measurements of x and $\dot{m}$ were obtained from manufacturers' product specifications. The thermocouples were calibrated using a NIST traceable RTD (Appendix A). Uncertainty in estimated variables was calculated using a sequential perturbation method. The uncertainties are reported as absolute values and as a percentage of local value. Curve fit errors were the main contributors of error in temperature measurement.

Table 4.1: Uncertainties in measured and estimated variables

Measured Variable	Total Error	Estimated Variable	Total Error
x (μm)	10	Re	0.12 %
T_w, $T_{b,in}$ (°C)	0.91 (Re = 204) 1.33 (Re = 251) 1.04 (Re = 285) 0.60 (Re = 297)	Nu	12 % (Re = 204) 13.5 % (Re = 251) 12 % (Re = 285) 7.5 % (Re = 297)
$T_{b,ex}$, T_{sur} (°C)	0.15		
$\dot{m}$ (kg/s)	0.12 %		

4.9: RESULTS AND DISCUSSION

Figure 4.5 shows the near-wall fluid temperature plotted against axial distance nondimensionalized with hydraulic diameter. Note that the inlet temperature decreases with increase in Re due to the decrease in preheating inside the reservoir. The temperature profile as expected shows first a steep nonlinear and then a linear rise from entry to exit. Figure 4.6 shows local Nu profile along the length of the channel. The estimated Nu is compared with the solution for fully developed Nu (Shah and London, 1978) with constant axial heat flux and constant peripheral channel wall temperature. A constant peripheral wall temperature assumption is more proper for single phase flows through Si channel because conductive thermal resistance is much lower than convective thermal resistance. As expected, the Nu profile takes a longer distance to reach fully developed value with increasing Re number. Figure 4.6 shows that the fully developed Nu obtained is overestimated with this technique. This can be attributed to the underestimation of actual inner wall surface temperature due to the measurement of an average fluid temperature close to the wall.

Figure 4.7 shows variation of Nu with x*. Note that the two higher Pe cases do not collapse on low Pe curves. This could be due to the axial conduction effects. It is expected that the length of the thermally developing region increases with Pe. Because the thermally developing flow region has a higher heat transfer coefficient, more heat is conducted axially to this region giving rise to a non-uniform axial heat flux boundary condition.

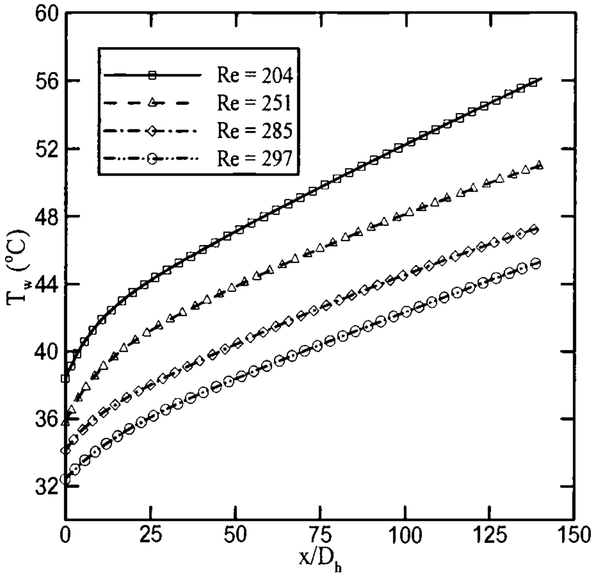

Fig. 4.5: Axial variation of near-wall fluid temperature T_w distribution.

To account for this axial conduction effect, measurements of the heat sink top surface temperature were recorded at identical flow conditions. The axial variation in heat flux was assumed to be similar to the axial variation in the difference between the heat sink top surface temperature and the fluid top interface temperature as indicated in Eq. 4.14. The heat sink top surface temperature and fluid interface temperature profiles are shown in Fig. 4.8 for the two higher Pe cases. Figure 4.9 compares Nu profiles for the varying axial heat flux boundary condition with that obtained with constant axial heat flux boundary condition. Note that the Nu values for the varying case are higher than that for constant heat flux condition. Also, the difference in Nu distribution for two different boundary conditions is small for lower Pe number case. This suggests that for lower Pe number single phase flows through Si channels, the thermally developing length is small and the boundary conditions of constant heat flux axially and constant peripheral temperature can be assumed as a good approximation.

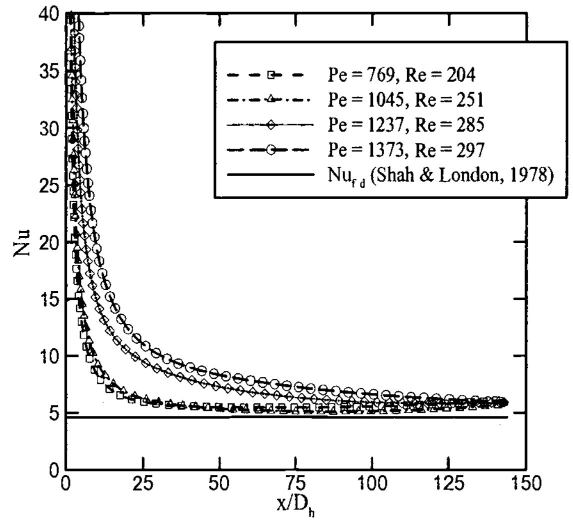

Fig. 4.6: Axial variation of Nu assuming a constant heat flux applied in the axial direction. The laminar fully developed flow solution is shown for the case of axially constant heat flux and peripherally constant channel wall temperature.

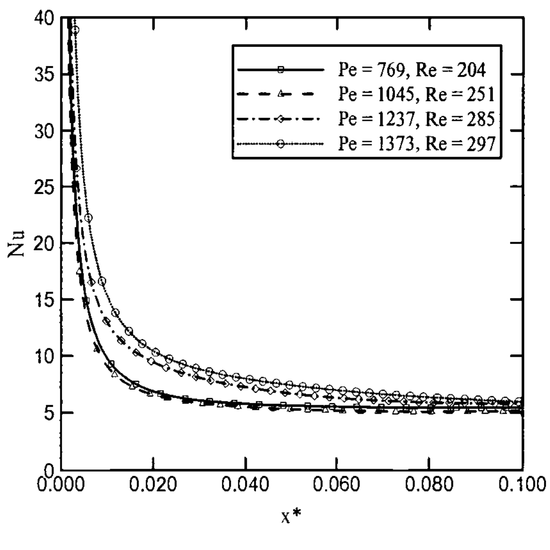

Fig. 4.7: Variation of Nu along the microchannel with x*. A constant axial heat flux and peripherally constant channel wall temperature is assumed.

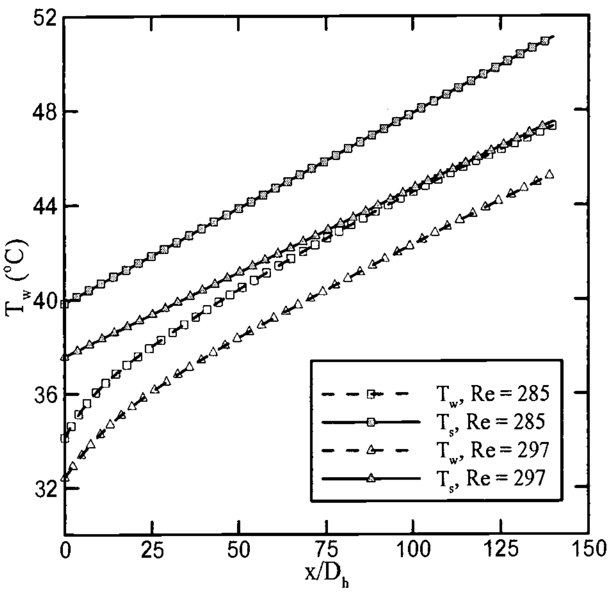

Fig. 4.8: Axial variation of near-wall fluid temperature, T_w, and heat sink surface temperature, T_s, along the microchannel, indicating existence of variable heat flux along the axial direction.

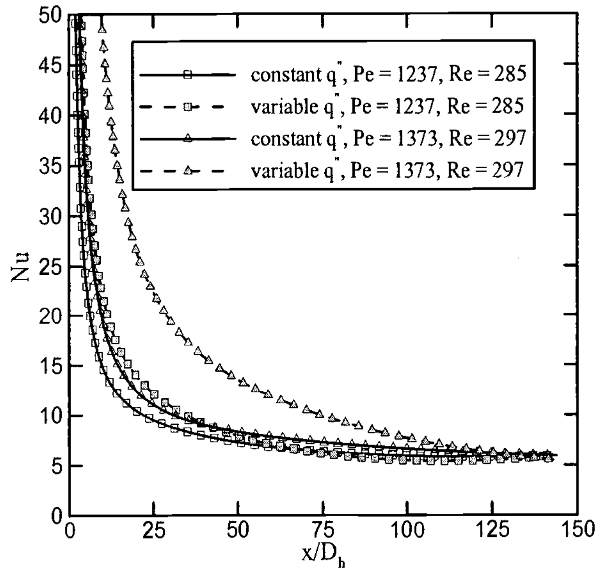

Fig. 4.9: Comparison of the axial variation of Nu along the microchannel for constant and variable axial heat flux. The peripheral wall surface temperature, T_w, at any location is assumed to be constant.

4.10: CONCLUSIONS

A new method of determining wall surface temperature in microchannels fabricated in Si heat sinks has been described. The experimental and data analysis procedure has been presented, and the technique validated for single phase laminar water flows. Uncertainties in estimated local Nu ranged between 7.5 percent to a maximum of 13.5 percent in the experimental range. This technique can, in general, be used for non-intrusive temperature measurement of single-phase gas and liquid microchannel wall, or near-wall liquid, temperatures.

Results for a 50 μm wide by 135 μm deep all-Si side wall microchannel indicates close agreement of the experimentally determined Nu in the fully developed region to the solution in the literature (Shah and London, 1978). The heat flux was found to vary in the axial direction for large Reynolds numbers, while a constant axial heat flux approximation is found to be fairly accurate for lower Reynolds numbers in the range of parameter variation in this study.

CHAPTER 5: CONCLUSIONS

A novel method of determining local heat transfer rates in microscale flows using microscopic IR thermography has been described. The technique was applied to study heat transfer characteristics for single-phase external and internal flows. Experimental and data analysis procedures required to obtain heat transfer measurements from the technique were presented.

In the context of external flow, microscale axisymmetric jet impingement heat transfer was studied experimentally. The jet flow was confined and submerged, and issued from a nozzle with a cross-sectional diameter of 125 μm. Experiments were performed for five Reynolds numbers between 690 and 1770 (corresponding M ranged between 0.26 and 0.63) for three H/D ratios of 2, 4 and 6. Average Nu obtained in this study were significantly higher for higher Re compared to predictions using Martin's correlation (Martin, 1977). This was attributed to fluid compressibility and a possible slip flow regime along the impingement wall.

Microscale internal flow through an all Si rectangular channel was studied using IR thermography. Near wall fluid temperatures for single phase laminar water flow over a Re range of 200 and 300 were mapped. Results for a 50 μm wide by 135 μm deep all-Si side wall microchannel indicates close agreement of the experimentally determined Nu in the fully developed region to the solution in literature (Shah and London, 1978). Heat flux was found to vary in the axial direction for large Reynolds numbers, while a constant axial heat flux approximation was found to be fairly accurate for lower Reynolds numbers in the range of experiments performed in this study.

CHAPTER 6: RECOMMENDATIONS FOR FUTURE WORK

Microscale jet impingement:

1. The frequency of recordings and spatial resolution (~10 μm) of the IR camera is not good enough to do detailed studies in the stagnation region of heat transfer for a microscale jet. The spatial resolution achieved by unsealed thermochromic liquid crystals imaging (Hohmann et al., 2002) is roughly one order of magnitude (~1 μm) better than that achieved by IR camera and hence it could be a better instrument to study microscale jet impingement.
2. Low thermal conductive impingement foil should be used to get local distribution of the recovery factor for varying Re. This experiment could confirm the existence of slip flow regime in microscale jet impingement along the impingement surface. Pence et al. (2003) have shown that the slip flow boundary condition displaces the local minima in the recovery factor away from stagnation point.
3. If possible, flow visualization studies could help confirm and show clearly the spread of microjets with varying H/D.
4. A low thermal conductive foil reduces the lateral conduction and hence will reduce the uncertainties in heat transfer rate estimates.
5. The contact resistance between copper foil and impingement foil, which was comparable to the foil resistance, should be reduced.
6. The impingement foil area should be reduced to same order of magnitude as the jet diameter.

Microscale internal flow:

1. The experiments should be conducted with channel having large axial length to diameter ratio for varying Re. This would make the assumption of uniform axial heat flux distribution more correct and hence the technique could be further validated.
2. The experiments should be conducted with varying channel hydraulic diameters and changes in the entry length region should be noted.
3. More exhaustive radiation analysis is needed to correctly estimate the effective path length for emission and if possible to determine a correction factor to estimate the wall temperature accurately.
4. More experiments with varying Pe should be performed and effect of conduction in Si on axial heat flux distribution should be documented.

BIBLIOGRAPHY

Astarita T., Cardone G., Carlomagno G.M. and Meola C., 2000, A Survey of Infrared Thermography for Convective Heat Transfer Measurements, Optics and Laser Technology, Vol. 32, pp 593-610.

Buffone C. and Sefiane K., 2004, IR Measurements of Interfacial Temperature during Phase Change in a Confined Environment, Experimental Thermal and Fluid Science, Vol. 29, pp 75-74

Carlomagno G.M. and de Luca L., 1989, Infrared thermography in heat transfer, in: Handbook of Flow Visualization, ed. W. I. Yang, Hemisphere Publishing Corporation, Washington DC, 531-553.

Chatterjee and Deviprasad L., 2001, Heat Transfer in Confined Laminar Axisymmetric Impinging Jets at Small Nozzle-Plate Distances: The Role Upstream Vorticity Diffusion, Numerical Heat Transfer Part A, vol. 39, No. 8, pp 777-800.

Chung J., Shin Y., Petigrew K., Chapman P., Grigoropoulos C. and Grief R., 2001, Infrared Thermal Velocimetry, paper HTD 24410, CD-ROM Proceedings of 2001 ASME IMECE, New York, NY.

Donaldson C.D., Snedeker R.S. and Margolis D.P., 1971, A Study of Free Jet Impingement. Part 2. Free Jet Turbulent Structure and Impingement Heat Transfer. Journal of Fluid Mechanics, Vol. 45, No. 3, pp 477-512.

Figliola R. and Beasley D., 2000, Theory and Design for Mechanical Measuremants, 3rd edition, John Wiley & sons.

Fletcher D. A., Kino G. S. and Goodson K. E., 2003, Thermal Microscopy with a Microfabricated Solid Immersion Lens, Microscale Thermophysical Engineering, Vol. 7, No. 4, pp 267-273

Ghiaasiaan S. M., and Abdel-Khalik S. I., 2001, Two-Phase Flow in Microchannels, Advances in Heat Transfer, Vol. 34, pp. 145-254.

Goldstein R.J., Behbahani A.I. and Heppelmann K.K., 1986, Streamwise Distribution of Recovery Factor and the Local Heat Transfer Coefficient to an Impinging Circular Air Jet, International Journal of Heat and Mass Transfer, Vol. 29, No. 8, pp. 1227–1235.

Goodson K.E. and Asheghi M., 1997, Near-Field Optical Thermography Microscale Thermophysical Engineering, vol. 1, pp. 225-235.

Han, G., Bird, J. C., Johan, K., Westin, A., Cao, Z., and Breuer, K. S., 2004, Infrared diagnostics for measuring fluid and solid motion inside silicon microdevices, Microscale Thermophysical Engineering, Vol. 8, pp. 169-182.

Hapke I., Hartwig B. and Schmidt J., 2002, Flow Boiling of Water and n-Heptane in Microchannels, Microscale Thermophysical Engineering, Vol. 6, No. 2, pp 99-115

Hassan, I., Phutthavong, P., and Abdelgawad, M., Microchannel heat sinks: An overviewof the state-of-the-art, Microscale thermophysical engineering, Vol. 8, No. 3, pp. 183-205, 2004.

Hestroni G., Rozenblit R. and Yarin L.P., 1996, A Hot-Foil Infrared Technique for Studying the Temperature Field of a Wall, Meas. Sci. Technol., vol. 7, pp. 1418-1427.

Hestroni, G., Mosyak, A., and Segal, Z., 2001, Nonuniform temperature distribution in electronic devices cooled by flow in parallel channels, IEEE Transactions on components and packaging technologies, Vol. 24, No. 1, pp. 16-23.

Hestroni, G., Mosyak, A., Segal, Z., and Pogrebnyak, E., 2003, Two-phase flow patterns in parallel micro-channels, International Journal of Mulitphase Flows, Vol. 29, pp. 341-360.

Hohmann C. and Stephan P., 2002, Microscale Temperature Measurement at an Evaporating Liquid Meniscus, Experimental Thermal and Fluid Science, Vol. 26, pp 157-162.

Hollingworth, K. D., 2004, Liquid Crystal Imaging of Flow Boiling in Minichannels, Paper # ICMM2004-2320, Proceedings of the 2nd International Conference on Microchannels and Minichannels (ICMM 2004), Rochester, NY., pp. 57-66.

Horny N., 2003, FPA camera standardization, Infrared Physics & Technology, vol. 44, pp. 109-119.

Jiang, L. and Wong, M., and Zohar, Y., 2001, Forced Convection Boiling in a Microchannel Heat Sink, Journal of Microelectromechanical Systems, 10, No. 1, pp. 80-87.

Kandlikar, S., 2002, Fundamental Issues Related to Flow Boiling in Minichannels and Microchannels, Experimental and Thermal Fluid Science, Vol. 26, pp. 389-407.

Kays W.M. and Crawford M.E., Convective Heat and Mass Transfer, Chapter 16, 3rd edition, McGraw-Hill, Inc., Hightstown, NJ.

Koo, J. M., Jiang, L., Zhang, L., Zhou, P., Banerjee, S. S., Kenny, T. W., Santiago, J. G., Goodson, K. E., "Modeling of two-phase microchannel heat sinks for VLSI chips," IEEE International conference on micro electro mechanical systems, pp. 422-426, 2001.

Kreith F. and Bohn M.S., 2000, Principles of Heat Transfer, Chapter 4, 6th edition, Thomson Learning, Stamford, Connecticut.

Lin Q., Wu S., Yuen L., Tai Y-C and Ho C-M, 2000, MEMS impinging-jet cooling, Proceedings of ASME 2000, MEMS-vol. 2, pp. 137-142.

Liu, D., Garimella, S. V., Wereley, S. T., 2004, Infrared Micro-Particle Image Velocimetry of fluid flow in Silicon-Based Microdevices, HT-FED04-56385, Proceedings of the 2004 ASME Heat Transfer/Fluids Engineering Summer Conference, Charlotte, NC.

Looney M.K. and Walsh J.J., 1984, Mean-Flow and Turbulent Characteristics of Free and Impinging Jet Flows, Journal of Fluid Mechanics, vol. 147, pp. 397-429.

Martin H., 1977, Heat and Mass transfer between Impinging Gas Jets and Solid Surfaces, Advances in Heat Transfer, vol. 13, pp. 1-60.

Meola C., de Luca L. and Carlomagno G.M., 1995, Azimuthal instability in an impinging jet: adiabatic wall temperature distribution, Experiments in Fluids, vol. 18, pp. 303-310.

Page R. and Hill W Jr., 1996, Location of Transition in a Free Jet Region, AIAA Journal, vol. 4, No. 5, pp 944.

Palm, B., 2001, Heat Transfer in Microchannels, Microscale Thermophysical Engineering, Vol. 5, pp. 155-175.

Patil V.A. and Narayanan V., 2004, Surface Temperature Visualization and Heat Transfer in Microscale Jet Impingement, Paper 236, CD-ROM Proceedings of the 11th International Symposium on Flow Visualization, University of Notre Dame, Notre Dame, IA.

Patil V.A. and Narayanan V., 2005a, Application of Heated-Thin-Foil thermography technique to external convective microscale flows, Measurement Science and Technology, vol. 16, pp. 472-476.

Patil V.A. and Narayanan V., 2005b, Spatially-Resolved Heat Transfer Rates in An Impinging Circular Microscale Jet, in press, Microscale Thermophysical Engineering.

Pence D. V., Boeschoten P. and Liburdy J. A., 2003, Simulation of Compressible Micro-Scale Jet Impingement Heat Transfer, Journal of Heat Transfer, Vol. 125, No. 3, pp. 447-453.

Peng, X. F., and Peterson, G. P., 1994, Heat transfer characteristics of water flowing through microchannels, Experimental Heat Transfer, Vol. 7, pp. 265-283.

Popescu, A., Welty, J. R., Pfund, D., and Rector, D., 2002, Thermal Measurements in Rectangular Micorchannels, Paper # IMECE2002-32442, Proceedings of IMECE 2002, New Orleans, LA.

Qu, W., and Mudawar, I., 2003, Flow boiling heat transfer in two-phase micro-channel heat sinks-I Experimental investigation and assessment of correlation methods, International Journal of Heat and Mass Transfer, Vol. 46, pp. 2755-2771.

Rainieri S. and Pagliarini G., 2002, Data Processing Technique Applied to the Calibration of a High Performance FPA Infrared Camera, Vol. 43, pp. 345-351.

Rogalski A., 2002, Infrared Detectors: An Overview, Infrared Physics & Technology, vol. 43, pp. 187-210.

Saad N., Douglas W. and Mujumdar A., 1977, Prediction of Heat Transfer under an Axisymmetric Laminar Impinging Jet, Ind. Eng. Chem., Fundam, Vol. 16, No. 1, pp 148-154.

Sargent S.R., Hedlund C.R. and Ligrani P.M.., 1998, An infrared thermography imaging system for convective heat transfer measurements in complex flows Meas. Sci. Technol., Vol. 9, pp. 1974-1981.

Siegel, R. and Howell, J.R., 2002, Thermal Radiation Heat Transfer, 4th edition, Hemisphere Publishing Co., Washington, DC.

Shah, R. K. and London A. L., 1978, Laminar Flow Forced Convection In Ducts, Supplement 1 to Advances in Heat Transfer, Academic, New York.

Shapiro, 1993, The dynamics and thermodynamics of compressible fluid flow-Vol. 2, Chapter 26, first edition reprint, R. E. Krieger Publishing Co., Malabar, Florida, 1985.

Tso, C. P., and Mahulikar, S. P., 2000, Experimental verification of the role of Brinkman number in microchannels using local parameters, Int. Journal of Heat and Mass Transfer, Vol. 43, pp. 1837-1849.

Tuckerman D.B. and Pease, R.F.W., 1981, High Performance Heat Sinking for VLSI, IEEE Electron Device Letters, ED1-2, pp. 126-277.

Viskanta R., 1993, Heat Transfer to Impinging Isothermal Gas and Flame Jets, Experimental Thermal and Fluid Science, vol. 6, pp. 111-134.

Zhang, L., Koo, J-M., Jiang, L., Asheghi, M., Goodson, K., Santiago, J., and Kenny, T., 2002, "Measurements and Modeling of Two-Phase Flow in Microchannels With Nearly Constant Heat Flux Boundary Conditions," Journal of Microelectromechanical Systems, 11, 1, pp. 12-19.

APPENDIX A: CALIBRATION

Calibration of foil resistance

Foil resistance was calibrated by passing known current through the foil and measuring the voltage drop across the foil. The current was measured at the voltage source which was in series with the foil. The voltage drop across the foil was measured using a digital multimeter and a average of three values was used. The foil resistance was calculated using Ohm's law. Table A.1 tabulates the calibration data obtained using the above mentioned procedure.

Table A.1: Calibration data for the foil resistance.

Current (A)	Voltage (V)	Foil resistance (Ω)
0.5	0.358	0.716
0.75	0.445	0.593
0.999	0.5275	0.528
1.5	0.725	0.483
2	0.843	0.422

Equation (A.1) gives the calibration equation for resistance (R_f) versus current (I) supplied.

$$R_f = -0.2146.I^3 + 0.9311.I^2 - 1.3975.I + 1.2088 \tag{A.1}$$

Calibration of pressure transducer

The differential pressure transducer was calibrated using dead weight calibrator. The calibration data for pressure calibration are shown in table A.2.

Table A.2: Calibration data for the pressure measurement.

$P_{applied}$ (psi)	Voltage (V)	P_{eqn} (psi)	P_{eqn}-$P_{applied}$
50	13.845	50.05	0.002514
45	12.505	45.02	0.000429
40	11.145	39.92	0.007018
35	9.835	34.99	3.53E-07
30	8.475	29.90	0.011042
25	7.133	24.86	0.020167
20	5.805	19.87	0.015786
15	4.712	15.77	0.594826
10	3.104	9.74	0.069726
5	1.809	4.88	0.015334
		Std deviation	0.286132
		t value	2.262
		Error	0.647 psi

The calibration equation for pressure versus voltage output of transducer is given by equation (A.2)

$$P = 3.7533.V - 1.9143 \tag{A.2}$$

Calibration of thermocouples

The thermocouples were calibrated using a NIST traceable RTD. The calibration data for the two thermocouples used are shown in table A.3.

Table A.3: Calibration data for the thermocouple (K type).

$T_{RTD,1}$ (°C)	$T_{thermocouple,1}$ (°C)	$T_{RTD,2}$ (°C)	$T_{thermocouple,2}$ (°C)
30.36	30.41	30.03	30.03
35.28	35.19	35.28	34.9
40.1	40.16	40.1	39.96
44.92	44.94	44.92	44.92
49.99	49.92	49.99	49.99
69.92	69.94	69.92	69.84
Curve fit error	0.165	Curve fit error	0.11
Bias error	0.1	Bias error	0.1
Total error	0.2	Total error	0.15

APPENDIX B: UNCERTAINTY CALCULATIONS FOR JET IMPINGEMENT STUDY

Uncertainty in Reynolds number

The uncertainty in flow rate ($\dot{Q}$) measurement was obtained from the calibration charts provided by the manufacturer and it was ±6.73 ml/min for the rotameter used. The Reynolds number at nozzle exit is given by equation B.1.

$$\mathrm{Re} = \left(\frac{4.\dot{Q}}{\pi.D^2} \right) . \frac{D}{\nu} \qquad \text{(B.1).}$$

Using propagation of error, the uncertainty in Reynolds number determination was found out to be ±71.86.

Uncertainty in T and T_{aw}

The uncertainty calculations for T and T_{aw} are tabulated in table B.1. Here, U is the error value and the subscript stands for type of error.

Table B.1: Uncertainty calculation for T and T_{aw}

	$U_{sensitivity}$	$U_{resolution}$	$U_{curvefit}$	$U_{precision}$	Total error
T (°C)	0.05	0.01	0.15	0.231	0.28
T_{aw} (°C)	0.05	0.01	0.15	0.268	0.31

Uncertainty in foil area (A_{foil}) and q''_{gen}

The length and breadth of the foil was measured using vernier calipers which had a resolution error of 0.02 mm. The error in area estimation was found to be 0.267

mm^2. The uncertainty in measurement of I and R_{foil} are reported in Table 2.2 and were estimated from manufacture's catalog and calibration respectively. The uncertainty in q''_{gen} can be estimated using equation (2.4) and propagation of errors and has been reported in table 2.3.

Uncertainty in Nu and Nu_{av}

Uncertainty in Nu and Nu_{av} was found using perturbation technique wherein the variables affecting the Nu and Nu_{av} were perturbed by their uncertainty value and the corresponding perturbation in Nu and Nu_{av} were noted. Finally these perturbations in estimated variable were root sum squared to obtain the total uncertainty value.

Table B.2 shows the perturbation analysis applied to estimate error in Nu for Re = 690 and 1770 case at r = 0.

Table B.2: Sample uncertainty calculation for Nu

	Perturbed Variables					
	T	T_{aw}	q''_{gen}	q''_{cond}	Curve fit error	Total error
Nu (Re = 690)	0.26	0.32	0.17	1.03	0.09	1.126 (8.1%)
Nu (Re = 1770)	2.2	2.7	0.38	4.79	0.3	5.95 (10.4%)

APPENDIX C: H/D VARIABILITY

The following figures show the non-dimensional adiabatic and heated temperature distributions for Re = 970, 1620 and 1770 with varying H/D of 2, 4 and 6.

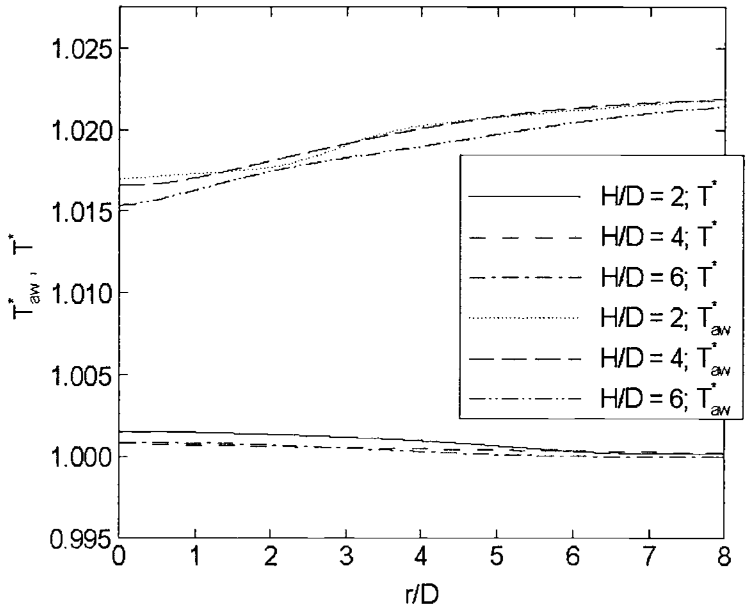

Fig. C.1: Non-dimensional adiabatic and heated wall temperature distribution for Re = 970

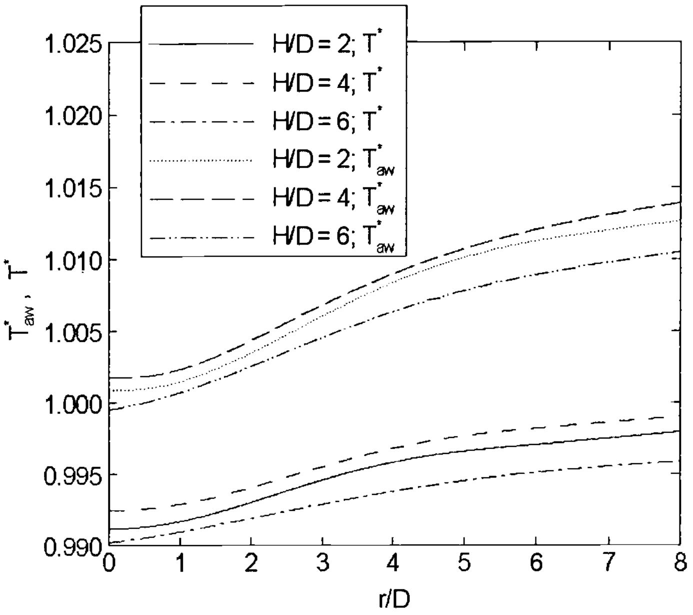

Fig. C.2: Non-dimensional adiabatic and heated wall temperature distribution for Re = 1620

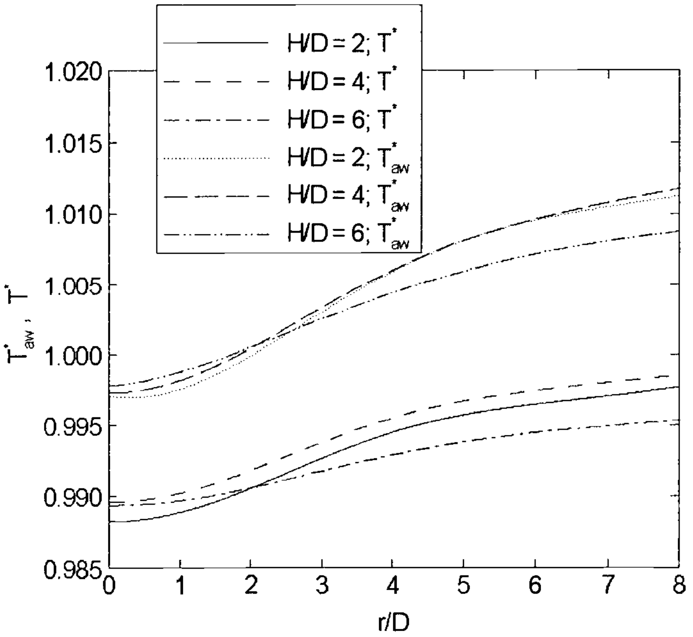

Fig. C.3: Non-dimensional adiabatic and heated wall temperature distribution for Re = 1770

APPENDIX D: UNCERTAINTY CALCULATIONS FOR INTERNAL FLOW STUDY

Uncertainty in Reynolds number

The uncertainty in mass flow rate ($\dot{m}$) measurement was obtained from the calibration charts provided by the manufacturer and it was ±0.12 % of the local value for the Coriolis meter used. The Reynolds number at nozzle exit is given by equation D.1.

$$Re = \left(\frac{4.\dot{m}}{\pi.D_h^2} \right) . \frac{D_h}{\nu} \tag{D.1}$$

Using propagation of error, the uncertainty in Reynolds number determination was found out to be ±0.12 %.

Uncertainty in estimating $\left(\varepsilon_f.\bar{T}\right)$ factor

Local $\left(\varepsilon_f.\bar{T}\right)$ factor was determined using equation D.2

$$\left(\varepsilon_f.\bar{T}\right) = \left(\frac{T_f}{T_{act}} \right)^4 \tag{D.2}$$

Here, T_{act} is the true temperature of water flowing through microchannel during calibration process and T_f is the temperature estimated by IR camera assuminf emissivity equal to one. T_{act} was measured using a wire thermocouple and the uncertainty in this measurement was 0.15 °C. Error in T_f was due to resolution error, sensitivity error and precision error in IR measurement (see next section) and was found out to be equal to ± 0.117 °C. Using propagation of errors, the error in estimating $\left(\varepsilon_f.\bar{T}\right)$ factor was found to be ±0.26 %.

Uncertainty in IR measurements (T_w and $T_{b,in}$)

The uncertainty calculations for temperature measurement using IR thermography are tabulated in table D.1. Here, U is the error value and the subscript stands for type of error.

Table D.1: Uncertainty in T_w for different Re

T_w (Re)	$U_{sensitivity}$	$U_{resolution}$	$U_{curvefit}$	$U_{\varepsilon_f \bar{T}}$ (max)	$U_{precision}$ (max)	Total error (°C)
T_w (204)	0.05	0.01	0.86	0.235	0.1	0.91
T_w (251)	0.05	0.01	1.3	0.235	0.1	1.33
T_w (285)	0.05	0.01	1	0.235	0.1	1.04
T_w (297)	0.05	0.01	0.54	0.235	0.1	0.607

Uncertainty in Nu

Uncertainty in Nu was found using perturbation technique wherein the variables affecting the Nu were perturbed by their uncertainty value and the corresponding perturbation in Nu was noted. Finally these perturbations in estimated variable were root sum squared to obtain the total uncertainty value. Table D.2 shows the above perturbation analysis applied to estimate error in Nu.

Table D.2: Uncertainty in Nu

Error in Nu (% local value)	Perturbed Variables			Total error (%)
	$T_{b,exit}$ (max)	T_w, $T_{b,in}$ (max)	$\dot{m}$	
Nu (Re = 204)	1.66	11.51	0.12	11.63
Nu (Re = 251)	1.81	13.4	0.12	13.53
Nu (Re = 285)	1.55	11.71	0.12	11.81
Nu (Re = 297)	2.02	7.65	0.12	7.65

APPENDIX E: PROCEDURE TO OBTAIN WALL TEMPERATURE ESTIMATES

The step by step procedure followed to obtain wall temperature measurements is shown for Re = 297 case. Figure E.1 shows the intensity map obtained during calibration wherein the water at 23.5 °C is flowing through channel. The intensity along the channel length for this image is shown in figure E.2. The axial variation of the combined $(\varepsilon_f.\overline{T})$ factor for this particular location is shown in figure E.3 and was obtained using equation E.1.

$$(\varepsilon_f.\overline{T}) = \frac{i_{det}}{\sigma.(T_{water})^4} \tag{E.1}$$

Here, T_{water} is the water temperature (°K) flowing through microchannel.

Note that the factor $(\varepsilon_f.\overline{T})$ (≈ 0.96) is close to that predicted by theory. The intensity map obtained for Re = 297 and q" = 18.87 W/cm^2 case is shown in figure E.4. The actual T_w obtained after applying the $(\varepsilon_f.\overline{T})$ correction is shown in figure E.5. The equation used to obtain T_w from the detected intensity is given by

$$T_w = \left(\frac{i_{det}}{\sigma.(\varepsilon_f.\overline{T})}\right)^{1/4} \tag{E.2}$$

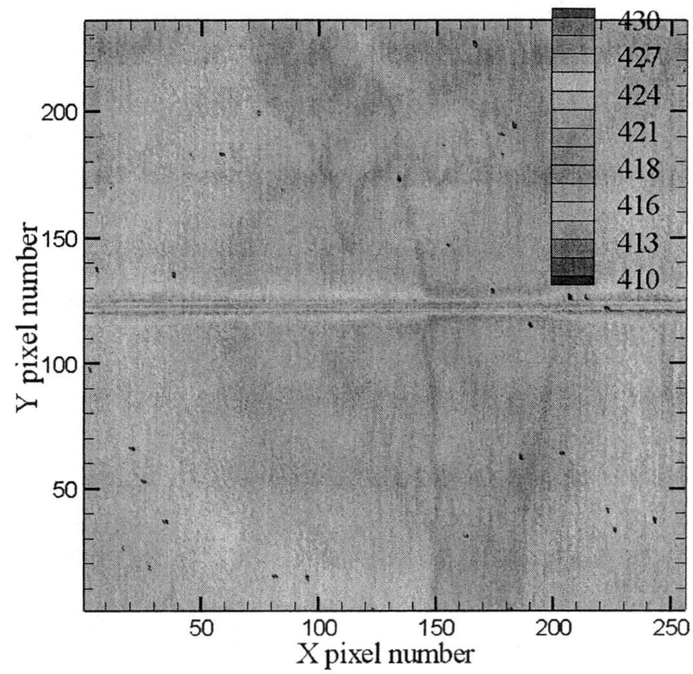

Fig. E.1: Typical intensity map obtained during calibration

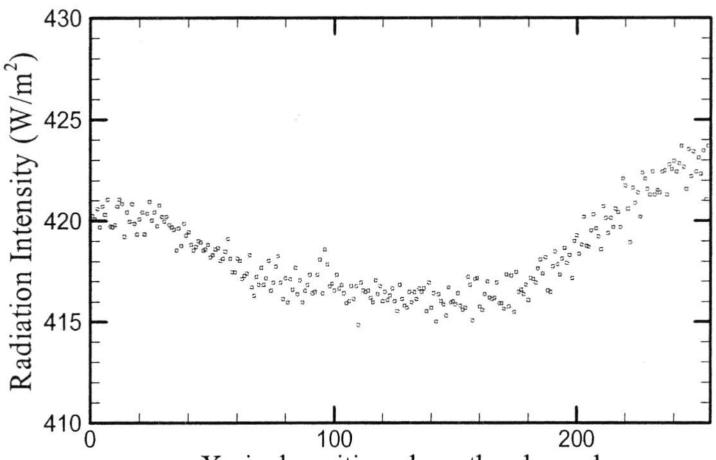

Fig. E.2: Axial variation of detected intensity along the channel length

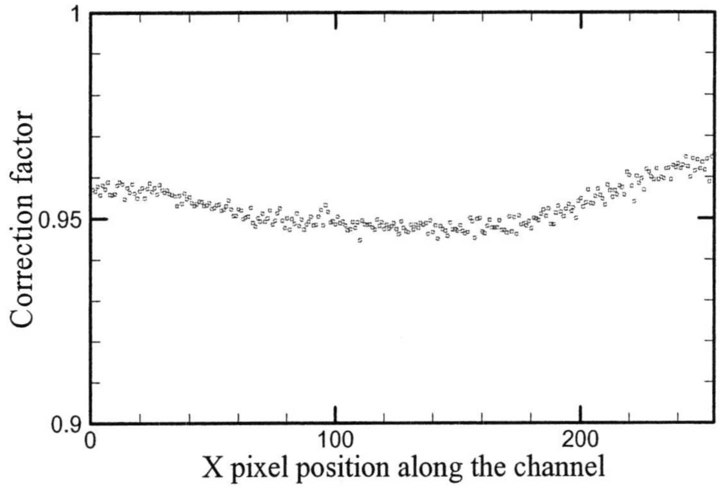

Fig. E.3: Axial variation of $\left(\varepsilon_f.\overline{T}\right)$ correction factor along the channel length

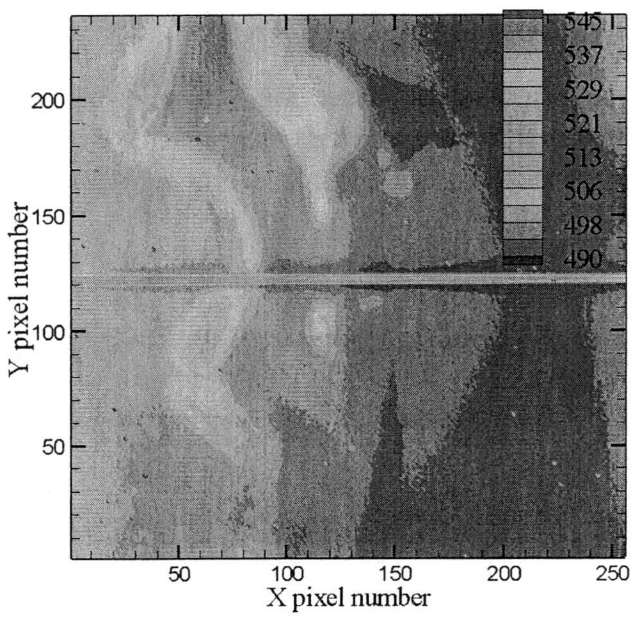

Fig. E.4: Typical intensity map obtained during test conditions

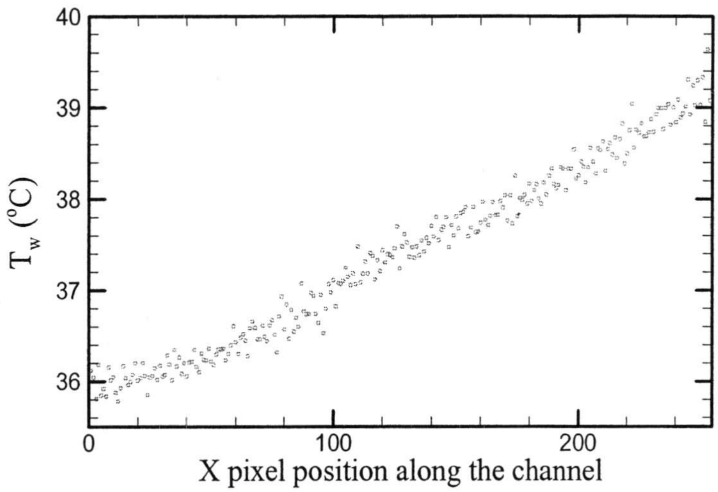

Fig. E.5: Plot of true T_w along the length of the channel

APPENDIX F: CHANNEL CROSS SECTIONAL DIMENSION

Figure F.1 shows the channel exit cross-section observed under a 40x objective. The picture was captured using a high sensitive camera system (Make: Hamamatsu photonics K.K., Model: C8484-52-05CP). Help received from Greg Mochka to capture this image is sincerely appreciated by the author

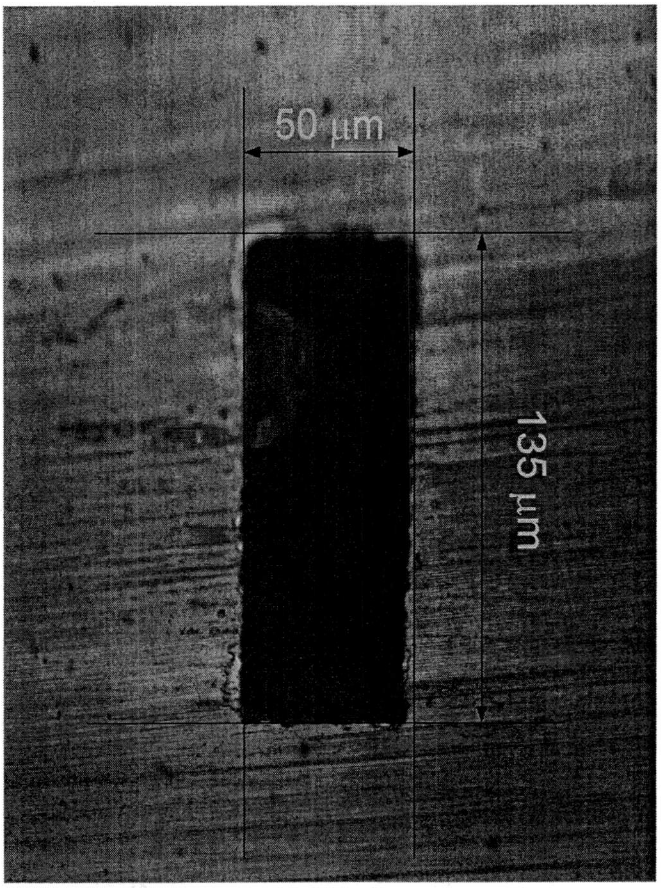

Fig. F.1: Channel exit cross section

Appendix G: Local data for 500 μm jet

Figure G.1 shows the local raw temperature distribution obtained for 500 mm jet impingement studies. The radial distribution of local Nu estimated is shown in fig. G.2.

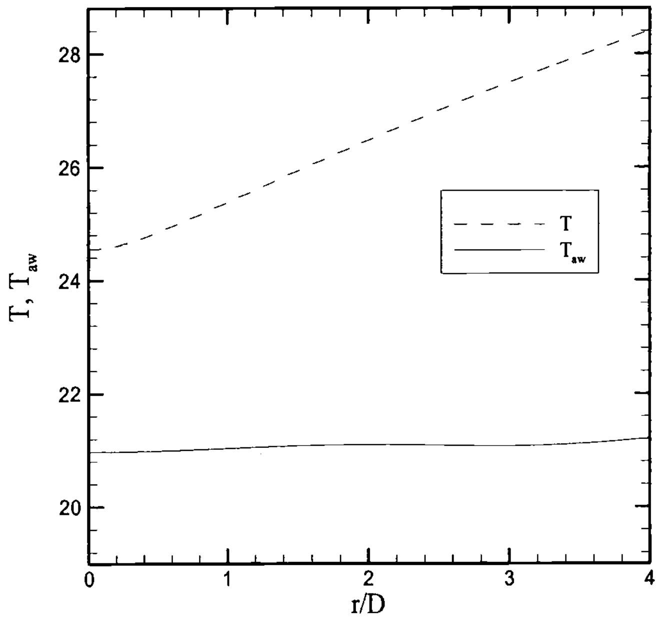

Figure G.1: Plot of local temperature distribution

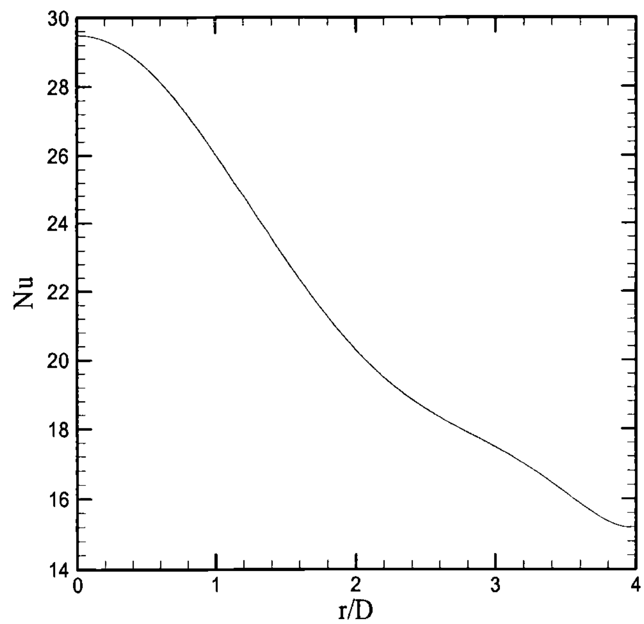

Figure G.2: Plot of local Nu distribution